



1 Variable tree rooting strategies improve tropical productivity and 2 evapotranspiration in a dynamic global vegetation model

3 Boris Sakschewski¹, Werner von Bloh¹, Markus Drüke¹, Anna A. Sörensson^{2, 3}, Romina Ruscica^{2, 3},
4 Fanny Langerwisch^{4, 5}, Maik Billing¹, Sarah Bereswill⁶, Marina Hirota^{7, 8}, Rafael S. Oliveira⁸, Jens
5 Heinke¹, Kirsten Thonicke¹

6 ¹Potsdam Institute for Climate Impact Research, Potsdam, 14473, Germany

7 ²Universidad de Buenos Aires - Consejo Nacional de Investigaciones Científicas y Técnicas, Centro de Investigaciones del
8 Mar y la Atmósfera (CIMA/UBA-CONICET), Buenos Aires, Argentina.

9 ³Institut Franco-Argentin d'Etudes sur le Climat et ses Impacts, Unité Mixte Internationale (UMI-IFAECI/CNRS-
10 CONICET-UBA), Argentina

11 ⁴Czech University of Life Sciences Prague, Department of Water Resources and Environmental Modeling, 165 00 Praha 6 –
12 Suchbátka, Czech Republic

13 ⁵Palacký University Olomouc, Department of Ecology and Environmental Sciences, 78371 Olomouc, Czech Republic

14 ⁶University of Potsdam, Potsdam, 14469, Germany

15 ⁷Federal University of Santa Catarina (UFSC), Campus Universitário Reitor João David Ferreira Lima Trindade –
16 Florianópolis – SC, CEP: 88040-900, Santa Catarina, Brazil

17 ⁸University of Campinas (UNICAMP) Cidade Universitária "Zeferino Vaz" CEP 13083-970, Campinas-SP, Sao Paulo,
18 Brazil

19

20

21 *Correspondence to:* Boris Sakschewski (boris.sakschewski@pik-potsdam.de)

22

23 **Abstract.** Tree water access via roots is crucial for forest functioning and therefore forests have developed a vast variety of
24 rooting strategies across the globe. However, Dynamic Global Vegetation Models (DGVMs), which are increasingly used to
25 simulate forest functioning, often condense this variety of tree rooting strategies into biome-scale averages, potentially
26 under- or overestimating forest response to intra- and inter-annual variability in precipitation. Here we present a new
27 approach of implementing variable rooting strategies and dynamic root growth into the LPJmL4.0 DGVM and apply it to
28 tropical and sub-tropical South-America under contemporary climate conditions. We show how competing rooting strategies
29 which underlie the trade-off between above- and below-ground carbon investment lead to more realistic simulated intra-
30 annual productivity and evapotranspiration, and consequently forest cover and spatial biomass distribution. We find that
31 climate and soil depth determine a spatially heterogeneous pattern of mean rooting depth and belowground biomass across
32 the study region.

33 1 Introduction

34 Tropical evergreen forest is the naturally dominant biome type in South-America over a large climatic range including
35 regions with a marked dry season (Hirota et al., 2011; Xiao et al., 2006). To withstand seasonal shortages of precipitation
36 and sustain productivity, trees with evergreen phenology often gain access to deep soil water via deep roots (Brum et al.,
37 2019; Canadell et al., 1996; Johnson et al., 2018; Kim et al., 2012; Markewitz et al., 2010). Consequently, recent studies
38 suggest a heterogeneous spatial pattern of maximum rooting depth across tropical forest biomes in South-America which
39 differs over the order of magnitudes depending on local groundwater, soil and climate conditions (Canadell et al., 1996; Fan
40 et al., 2017). Therefore, tree rooting depth is regarded as a crucial variable to explain the geographical distribution of main
41 phenology strategies such as “evergreen” and “deciduous”, as well as the observed local to continental pattern of
42 productivity, biomass storage, evapotranspiration (ET) and consequently moisture recycling (Fan et al., 2017; Jobbágy and
43 Jackson, 2000; Kleidon and Heimann, 2000; Langan et al., 2017; Nepstad et al., 1994; Stahl et al., 2013). While these
44 variables and processes are in the focus of model-based earth system sciences projecting the development of vegetation
45 formation and ecosystem functioning worldwide (Huntingford et al., 2013; Liu et al., 2018; Weber et al., 2009), most
46 DGVMs and land-surface models (LSMs) still do not represent the diversity of rooting depth or tree rooting strategies
47 (Warren et al., 2015a). In general these models condense the diversity of such functional plant traits to biome-scale averages,



48 to simulate so called plant functional types (PFTs) which reflect average plant individuals of a biome. Here, often a shallow
49 rooting depth for tree PFTs is assumed, i.e. most roots are distributed downwards to a few meters of depths at maximum
50 (Arora and Boer, 2003; Best et al., 2011; Guimberteau et al., 2017; Lawrence et al., 2011; Ostle et al., 2009; Schaphoff et al.,
51 2018; Smith et al., 2014). By ignoring natural local adaptations of rooting depth, DGVMs and LSMs in the past had
52 problems reproducing the extent of South-America's tropical evergreen forests, as well as its seasonal productivity and ET
53 especially in regions with seasonal rainfall (Baudena et al., 2014; Liu et al., 2018, 2017; Restrepo-Coupe et al., 2017).
54 So far different attempts were carried out trying to solve this problem in DGVMs and similar models by allowing for
55 variable rooting strategies. More than 20 years ago a pioneering study by Kleidon and Heimann (1998) systematically
56 searched for rooting strategies which yield highest net primary productivity over South America in a DGVM to explain intra-
57 annual rates of ET and vegetation cover. Follow up studies further underlined the importance of deep roots for the climate
58 system of South America (Kleidon and Heimann, 2000). Lee *et al.* (2005) found that allowing for deep roots and hydraulic
59 redistribution of water in the soil column in a general circulation model enhances Amazon forest productivity and
60 evapotranspiration (ET) in the dry season. Baker *et al.* (2008) came to similar results when introducing deep roots in a land
61 surface model. Ichii *et al.*, (2007) found that constraining rooting depth across the Amazon based on satellite data yields
62 similar results in a terrestrial ecosystem model. More recently, Langan, Higgins and Scheiter (2017) showed for the same
63 study area how diverse rooting strategies in a tree individual and trait-based DGVM can improve simulated intra-annual
64 productivity and ET and better explain patterns of different tropical biome types and biomass in connection with fire.
65 While these studies are important steps to acknowledge the diversity of tree rooting strategies and its effects, some
66 assumptions of the underlying models might decrease the liability of their results. These assumptions are related to 1)
67 resource investment, 2) timing and 3) physical constraints of rooting depth. 1) Most models so far do not account for coarse
68 roots (Warren et al., 2015a) even though they can make up the majority of total root biomass (Xiao et al., 2003). This
69 approach may be sufficient when employing shallow tree rooting strategies only, but with increasing rooting depth costs for
70 coarse roots increases substantially. Since the amount of resources trees can allocate to their processes and structures is
71 finite, a local adaptation of tree rooting depth must follow a trade-off between above- and below-ground resource investment
72 (Nikolova et al., 2011). Generally above-ground investments into leaf and stem growth can increase light absorption and
73 CO₂ uptake, while below-ground investments can increase the uptake of water and nutrients. Depending on local
74 environmental and competitive conditions one or the other direction might be more advantageous, eventually leading to
75 substantial regional variation in the mean below-ground to above-ground biomass ratios (Leuschner et al., 2007; Mokany et
76 al., 2006). Therefore, the simulated spectrum of tree rooting strategies which can survive and co-exist should be in
77 accordance with this crucial trade-off. 2) In contrast to above-ground stem growth, most DGVMs so far do not simulate
78 gradual root growth (Warren et al., 2015a). Instead PFTs are assigned a constant relative distribution of fine roots throughout
79 the soil column at any point in space and time (Best et al., 2011; Lawrence et al., 2011; Schaphoff et al., 2018; Smith et al.,
80 2014). As under the above mentioned simplification under 1), this approach may be sufficient when accounting for shallow
81 rooting strategies only, but when the maximum tree rooting depth of PFTs strongly diverges, it is questionable that the time
82 needed to reach this depth is negligible, especially when accounting for PFT competition. Rooting depth increases rather
83 gradually and non-linear over a tree's lifetime with a velocity driven by a mix of plastic optimization and allometric
84 determination (Brum et al., 2019; Brunner et al., 2015; Nikolova et al., 2011; Poorter et al., 2012; Warren et al., 2015b).
85 While the knowledge base for a mechanistic bottom-up modelling approach of plastic optimization is very sparse (Jenik,
86 2010; Poorter et al., 2012; Warren et al., 2015b), knowledge on certain allometric rules (Brum et al., 2019; Eshel and
87 Grünzweig, 2013; Mokany et al., 2006) seems enough to be applied in DGVMs. 3) Most DGVMs so far do not account for a
88 location dependent soil depth, but apply a constant soil depth across the globe (Best et al., 2011; Guimberteau et al., 2017;
89 Lawrence et al., 2011; Ostle et al., 2009; Schaphoff et al., 2018; Smith et al., 2014). Again this approach may be sufficient
90 when accounting for shallow rooting strategies only, but allowing for deep tree rooting strategies should go in parallel with



91 their potential physical barriers. Recent data products on global soil depth now enable to better constrain rooting depth in
92 DGVMs (Pelletier et al., 2016).
93 Here we overcome the above mentioned limitations and present a new approach of diversifying tree rooting strategies in the
94 DGVM LPJmL4.0 (Lund-Potsdam-Jena managed Lands; Schaphoff *et al.*, 2018) which increases the ecological liability
95 with the following aspects: 1) Maximum rooting depth is restricted to a recent global product of soil depth, 2) simulated tree
96 rooting strategies were chosen to represent a wide range of maximum rooting depth between 0.5 and 18 m, 3) this spectrum
97 of tree rooting strategies grows in competition and tree performance determines dominance, 4) dominance is supported by
98 best performing rooting strategies producing more offspring, 5) trees have to invest into coarse roots as well, i.e.
99 acknowledging the trade-off between growing deeper roots and allocating available carbon to other compartments (stem and
100 leaf growth), and 6) tree roots are growing deeper over time depending on tree height. The objectives of this study are to
101 describe an approach of how to diversify tree rooting strategies in a DGVM and to evaluate its effect on simulated
102 evapotranspiration, productivity, biomass and spatial distribution of evergreen and deciduous tropical forests using different
103 sources of validation data.

104 **2 Materials and Methods**

105 In the method sections below we describe the implementation of a new tree rooting scheme in LPJmL4.0 (Sect. 2.2) where
106 maximum rooting depth is constrained by a recent map on maximum soil/sediment thickness (Sect. 2.3). We apply the model
107 to several historical climate input data (Sect. 2.7) with details of the simulation protocol described in Sect. 2.9. The
108 Evaluation of the new model version is described in Sect. 2.10.

109 All data processing and statistical analysis described in the methods sections were performed with the commercial software
110 MATLAB® (MATLAB and Statistics Toolbox Release 2012b; The MathWorks, Inc., Natick, MA, USA).

111 **2.1 The LPJmL4.0 model**

112 LPJmL4.0 is a process-based Dynamic Global Vegetation Model (DGVM) which simulates the surface energy balance,
113 water fluxes, carbon fluxes and stocks of the global land (Schaphoff et al., 2018). Plant productivity is modelled on the basis
114 of leaf-level photosynthesis responding to climatic and environmental conditions, atmospheric CO₂ concentration, canopy
115 conductance, autotrophic respiration, phenology and management intensity. The model employs 11 plant functional types
116 (PFTs), 3 bioenergy types (BFTs) and 12 crop functional types (CFTs), to represent average plants of biomes, bioenergy
117 plantations and agriculture, respectively. The standard spatial resolution is a 0.5° x 0.5° grid. For each grid cell the fractional
118 coverage of bioenergy and agricultural BFTs and CFTs follows a prescribed land-use data set, whereas in the remaining area
119 natural PFTs grow in competition.

120 **2.2 A new tree rooting scheme for LPJmL4.0**

121 In this section we describe the new basic scheme for soil layer partitioning, the new tree rooting scheme, the simulation of
122 belowground carbon investment, and how different tree rooting schemes compete. All changes made to LPJmL4.0 described
123 in the methods below result in a new sub-version of LPJmL4.0 we call LPJmL4.0-VR hereafter (where “VR” stands for
124 variable roots).

125 **2.2.1 Scheme for soil layer partitioning**

126 LPJmL4.0 employs a globally universal soil depth of 3 m. For LPJmL4.0-VR we extended the general maximum soil depth
127 to 20 m (but restrict it to local soil depth information at spatial model resolution; Sect. 2.3.2). We applied the same basic
128 scheme for soil layer partitioning from LPJmL4.0 (Schaphoff et al., 2018), but continue this scheme down to 20 m (Tab. 1).



129 We chose a maximum of 20 m soil depth to considerably increase the maximum soil depth compared to constant 3 m in
130 LPJmL4.0, while keeping the increment of computational intensiveness connected to adding more soil layers within an
131 acceptable range. As for LPJmL4.0, a general soil texture information is applied to the whole soil column (Schaphoff et al.,
132 2018).

133 2.2.2 Diversifying general tree rooting strategies in LPJmL4.0-VR

134 In LPJmL4.0 the tree rooting strategy of a PFT is reflected by a certain prescribed vertical distribution of fine roots
135 throughout the soil column. Each soil layer l is assigned a PFT specific relative amount of fine roots $rootdist_l$:

$$136 \quad rootdist_l = rootdist(z_l) - rootdist(z_{l-1}) \quad \text{Eq. (1)}$$

137 where z_l is the soil layer boundary depth in cm of each soil layer l and $rootdist(z_l)$ is the relative amount of fine roots between
138 the forest floor and the boundary of soil layer l . The function $rootdist(z)$ is defined following Jackson *et al.* (1996):

$$139 \quad rootdist(z) = \frac{1 - \beta^z}{1 - \beta^{z_{bottom}}} \quad \text{Eq. (2)}$$

140 where β is a constant parameter shaping the vertical distribution of fine roots and therefore determining the tree rooting
141 strategy and z_{bottom} is the maximum soil depth in cm. In LPJmL4.0 each PFT is assigned a different β -value reflecting the
142 average tree rooting strategy on this broad biome scale (Schaphoff et al., 2018).

143 To quantify the maximum rooting depth of PFTs that actually results from this approach (Eq. 1&2) we here calculate the
144 depth which is reached by 95% of the fine root biomass (D_{95_max}) as follows:

$$145 \quad D_{95_max} = \frac{\log(1 - 0.95 \cdot (1 - \beta^{z_{bottom}}))}{\log(\beta)} \quad \text{Eq. (3)}$$

146 In LPJmL4.0 the β -values of tropical tree PFTs are set to 0.962 for the evergreen PFT and 0.961 for the deciduous PFT.
147 According to Eq. 3 both PFTs have a D_{95_max} smaller than 1 m. For LPJmL4.0-VR we extended this representation of tree
148 rooting strategies by splitting both tropical tree PFTs into 10 sub-PFTs and assigned each with a different β -value. These
149 values were chosen to cover a range of different D_{95_max} values between 0.5 and 18m (Tab. 2). Fig. 1 shows the new
150 maximum distribution of fine roots throughout the soil column according to the chosen β -values (Tab. 2).

151 2.2.3 Belowground carbon investment

152 Tropical trees can avoid water stress under seasonally dry climate by growing relatively deep roots (Brum et al., 2019; Fan et
153 al., 2017) which goes along with increased below-ground carbon investment. Thus, the need for deep water access creates a
154 trade-off between below-ground and above-ground carbon investment. Therefore, a new tree rooting scheme for LPJmL4.0-
155 VR was necessary to account for this trade-off in order to reproduce observed local to regional patterns and distributions of
156 tree rooting strategies instead of prescribing them. Therefore, we introduced two new carbon pools in LPJmL4.0-VR, namely
157 root sapwood and root heartwood. Like stem sapwood in LPJmL4.0, also root sapwood in LPJmL4.0-VR needs to satisfy the
158 assumptions of the pipe model (Shinozaki et al., 1964; Waring et al., 1982). The pipe model describes, that for a certain
159 amount of leaf area a certain amount of water conducting tissue must be available. In LPJmL4.0 the cross-sectional area of
160 stem sapwood needs to be proportional to the leaf area LA_{ind} as follows:

$$161 \quad LA_{ind} = k_{la:sa} \cdot SA_{ind} \quad \text{Eq. (4)}$$

162 where $k_{la:sa}$ is a constant describing the ratio of leaf area and stem sapwood cross-sectional area (SA_{ind}). In LPJmL4.0-VR we
163 also apply the pipe model to root sapwood. Root sapwood cross-sectional area must be proportional to stem sapwood cross-
164 sectional area, but is decreasing with soil depth, depending on the relative amount of fine roots in each soil layer (Fig. 2).
165 Root sapwood is turned into root heartwood at an equal rate as stem sapwood is turned into stem heartwood, i.e. 5% per year
166 as in LPJmL4.0 (see Schaphoff *et al.*, 2018).



167 2.2.4 Root growth

168 In LPJmL4.0 (Schaphoff et al., 2018) no vertical root growth is simulated, thus the relative distribution of fine roots over the
169 soil column is constant over space and time. It means that PFTs starting from bare ground in a sapling stage display the same
170 relative distribution of fine roots throughout the soil column as a full-grown forest which contradicts the principles of
171 dynamic root growth over a tree's lifetime. Applied to LPJmL4.0-VR, the belowground biomass of an initialized deep
172 rooting-strategy sub-PFT would exceed its aboveground biomass (AGB) by order of magnitudes when acknowledging
173 coarse roots. Consequently, deep rooting strategies would always be disadvantageous, calling for modelling gradual root
174 growth in LPJmL4.0-VR. Unfortunately, little is known about how roots of tropical trees grow over time, given the fact that
175 this research field is strongly time and resource demanding, and at the same time the variety of tree species, rooting
176 strategies and environmental conditions are large (Jenik, 2010). A recent promising study by Brum *et al.* (2019) was able to
177 capture the effective functional rooting depth (EFRD) of different size classes of 12 dominant tree species in a seasonal
178 Amazon forest where tree roots grow considerably deep with maximum values reaching below 30m. To our knowledge this
179 is the only study capturing the relation between the size of tropical trees and their maximum rooting depth in a high spatial
180 resolution covering sufficient tree-height classes in order to derive a function. Following the findings of Brum *et al.* (2019),
181 we here implemented a logistic root growth function, which calculates a general maximum conceivable tree rooting depth D
182 depending on tree height:

$$183 \quad D = \frac{S}{e^{-kSh}} \cdot \left(\frac{S}{D_0} - 1 \right) \quad \text{Eq. (5)}$$

184 where S is the maximum soil depth in the model (20 m), k is the growth rate (set to 0.02), h is the tree height in m and D_0 is
185 the initial rooting depth of tree saplings (set to 0.1 m; tree saplings in LPJmL4.0-VR are initialized with a height of 0.45 m as
186 in LPJmL4.0). The distribution of fine root biomass of each sub-PFT in the soil column is then adjusted according to D each
187 time step, by restricting z_{bottom} in Eq. 2. Every time D crosses a specific soil layer boundary (Sect. 2.2.1) z_{bottom} is assigned the
188 value of the next soil layer boundary. Thus, z_{bottom} increases in discrete steps. Consequently, each tree rooting strategy
189 allowed for in this study (2.2.2) shows a logistic growth of rooting depth dependent on tree height which saturates towards
190 its specific maximum rooting depth (Fig. 3). Therefore, limitations of aboveground tree growth due to below-ground carbon
191 investment of different tree rooting strategies (Sect. 2.2.3) are equal in the tree sapling phase of all sub-PFTs) and start to
192 diverge with increasing tree height. In the case D exceeds the grid cell specific local soil depth (as prescribed by the soil
193 thickness input, see Sect. 2.3.2) all the respective fine root biomass exceeding this grid cell specific soil depth is transferred
194 to the last soil layer which matches this soil depth (see also Fig. 2 right panel and Supplementary Video 1 for a visualization
195 of root growth under http://www.pik-potsdam.de/~borissa/LPJmL4_VR/Supplementary_Video_1.pptx).

196 The parameter k in Eq. 5 was chosen to preserve the slope of the 75%ile function describing the relation between tree height
197 and effective functional rooting depth (EFRD) as found in Brum *et al.* (2019). We could not implement any of the original
198 functions as suggested in Brum *et al.* (2019) since they deliver unrealistic low values of rooting depth (between 0 and 10cm)
199 for trees ≤ 10 m, which results in a strong competitive disadvantage against herbaceous PFTs in LPJmL4.0-VR. We
200 decided for the slope of the 75%ile function since we wanted to apply root growth rates close to the maximum which also
201 allows for the largest D_{95_max} values in this study (Sect. 2.2.1) to be reached.

202 Note that Brum *et al.* (2019) originally propose a relation between tree diameter at breast height (DBH) and EFRD. For our
203 purposes we related rooting depth to tree height (h), which is calculated from DBH in in LPJmL4.0 according to (Huang et
204 al., 1992):

$$205 \quad h = k_{allom2} \cdot DBH^{k_{allom3}} \quad \text{Eq. (6)}$$

206 where k_{allom2} and k_{allom3} are constants set to 40 and 0.67, respectively (Schaphoff et al., 2018).



207 2.2.5 Competition of rooting strategies

208 In each grid-cell all sub-PFTs of the evergreen and deciduous tree PFTs compete for light and water following LPJmL4.0's
209 approach to simulate plant competition. To allow for environmental filtering of tree rooting strategies which are best adapted
210 to local environmental conditions, we changed the tree establishment scheme of LPJmL4.0-VR. In LPJmL4.0, the number of
211 new PFT saplings per unit area (est_{PFT} in $\text{ind m}^{-2} \text{ a}^{-1}$) which are established each year is proportional to a maximum
212 establishment rate k_{est} and to the sum of foliage projected cover (FPC; a relative number between 0 and 1) of all tree PFTs
213 present in a grid cell (FPC_{TREE}). It declines in proportion to canopy light attenuation when the sum of woody FPCs exceeds
214 0.95, thus simulating a decline in establishment success with canopy closure (Prentice et al., 1993):

$$215 \quad est_{PFT} = k_{est} \cdot (1 - e^{(-5 \cdot (1 - FPC_{TREE}))}) \cdot \frac{1 - FPC_{TREE}}{n_{estTREE}} \quad \text{Eq. (7)}$$

216 where $n_{estTREE}$ is the number of established tree individuals per m^2 per year. In LPJmL4.0-VR, establishment rates of sub-
217 PFTs (est_{sub_PFT}) are additionally weighted by local dominance of each sub-PFT as follows:

$$218 \quad est_{sub_PFT} = k_{est} \cdot (1 - e^{(-5 \cdot (1 - FPC_{TREE}))}) \cdot \frac{1 - FPC_{TREE}}{n_{estTREE}} \cdot \frac{FPC_{sub_PFT}}{FPC_{TREE}} \cdot n_{estTREE} \quad \text{Eq. (8)}$$

219 where FPC_{sub_PFT} is the FPC of each sub-PFT. The new term allows productive sub-PFTs to establish more offspring relative
220 to their spatial dominance and vice versa, without changing the overall establishment rate as set by (Prentice et al., 1993).
221 This function has the effect that non-viable sub-PFTs are outcompeted over time.

222 2.2.5 Background mortality

223 In LPJmL4.0 background mortality is modelled by a fractional reduction of biomass, which depends on growth efficiency
224 (Schaphoff et al., 2018). This annual rate of mortality is limited by a constant maximum mortality rate of 3% of tree
225 individuals per year which is applied to all tree PFTs. In other words the fastest total biomass loss of a tree PFT due to low
226 growth efficiency can happen within $1/0.03 \sim 33$ simulation years. In general, this maximum mortality rate can be regarded
227 as a global tuning parameter of biomass accumulation as it caps the maximum biomass loss. Since many mechanisms
228 influencing tree mortality in the real world, e.g. hydraulic failure (Johnson et al., 2018), are not yet implemented in most
229 DGVMs including LPJmL4.0 (Allen et al., 2015), the parameterization of a background tree mortality remains a challenging
230 topic. Under the current model status of LPJmL4.0 maximum mortality rates are a necessary feature, while future model
231 development must overcome the concept of applying a maximum mortality rate by refining and implementing most
232 important mechanisms that influence tree mortality.

233 The new features of LPJmL4.0-VR head in this direction. Here tree PFTs can access water in soil depths which were
234 formally inaccessible. This enhances the general growth efficiencies of tree PFTs and consequently decreases their overall
235 background mortality. Since global biomass pattern simulated with LPJmL4.0 are already in an acceptable range, we
236 increased the maximum background mortality in LPJmL4.0-VR to 7% in order to counter-balance increased survival rates
237 and therefore biomass accumulation. This value keeps simulated mortality rates in real world boundaries, as a recent study
238 comprising data of 167 forest plots finds that actual annual stem mortality rates generally do not exceed 6% across Amazonia
239 (Johnson et al., 2016). We regard increasing the maximum mortality rate as a step into the right direction as its value can
240 eventually be set close to 100% when model development progresses.

241 2.3 Model input data

242 2.3.1 Climate and land-use input data

243 All versions of LPJmL used in this study (see Sect. 2.4) were forced with 4 different climate inputs each based on single or
244 multiple available data products delivering the climate variables air temperature, precipitation, long-wave and shortwave
245 downward radiation at daily or monthly resolution:



246 1) WATCH Forcing Data (WFD) + WATCH Forcing Data methodology applied to ERAInterim data. A combination of the
247 WATCH data set (Weedon et al., 2011) and the WFDEI data set (Weedon et al., 2014) as used in the ISIMIP project
248 (<https://www.isimip.org/gettingstarted/input-data-bias-correction/details/5/>). This input data set is called WATCH+WFDEI
249 hereafter.

250 2) Global Soil Wetness Project Phase 3 (GSWP3) (Kim *et al.*, no date; <http://hydro.iis.u-tokyo.ac.jp/GSWP3/index.html>).

251 3) NOAA Global Land Assimilation System version 2.0 (GLDAS, Rodell *et al.*, 2004).

252 4) Climate forcing as in Schaphoff *et al.* (2018) with monthly precipitation provided by the Global Precipitation Climatology
253 Centre (GPCC Full Data Reanalysis version 7.0; (Becker et al., 2013), daily mean temperature from the Climate Research
254 Unit (CRU TS version 3.23, University of East Anglia Climatic Research Unit, 2015; Harris *et al.*, 2014), shortwave
255 downward radiation and net downward radiation reanalysis data from ERA-Interim (Dee et al., 2011), and number of wet
256 days from (New et al., 2000) used to allocate monthly precipitation to individual days.

257 This input data set is called CRU hereafter.

258 2.3.2 Soil and sediment thickness

259 We regridded a global 1 x 1 km soil and sediment thickness product (Pelletier et al., 2016) to the 0.5° x 0.5° spatial
260 resolution of LPJmL4.0-VR, set the global maximum value to 20 m according to the maximum soil depth chosen for
261 LPJmL4.0-VR (Sect. 2.2.1), and used the resulting map as grid cell specific model input (Fig. 4).

262 2.4 Model versions and simulation protocol

263 In order to investigate the impact of simulating variable rooting strategies and root growth, we employ 3 model versions of
264 LPJmL in this study: 1) LPJmL4.0, 2) LPJmL4.0-VR, and 3) LPJmL4.0-VR-base with the same settings as LPJmL4.0-VR
265 but without variable rooting strategies, i.e. using the β -values of LPJmL4.0 for the tropical evergreen PFT ($\beta = 0.962$) and
266 the tropical deciduous PFT ($\beta=0.961$) for all the respective 10 sub-PFTs. We regard the latter model version as a baseline
267 model of this study, because comparisons to LPJmL4.0-VR enable to investigate differences which are caused by the amount
268 of considered tree rooting strategies only.

269 Each simulation was initialized with 5000 simulation years of spin up from bare ground without land-use by randomly
270 recycling the first 30 years of respective climate data (1901-1930 for WATCH+WFDEI, GSWP3, CRU and 1948-1977 for
271 GLDAS) and a pre-industrial atmospheric CO₂ level of 278ppm, in order to ensure that carbon pools and local distribution of
272 PFTs and sub-PFTs are in equilibrium with climate. This first spin-up phase was followed by another spin up phase of 390
273 years using the same climate data, but employing historical land-use data (reshuffling the first 30 years 1851-1880). Land-
274 use input and routines were carried out according to the standard settings of LPJmL 4.0 as described in (Schaphoff et al.,
275 2018). This second spin-up phase was followed by transient simulations (1901-2010 for WATCH+WFDEI, GSWP3, CRU
276 and 1948-2010 for GLDAS) with respective land-use change and changing levels of atmospheric CO₂ concentration.

277 At the beginning of the spin-up phase, all sub-PFTs in LPJmL4.0-VR and LPJmL4.0-VR-base have the same chance to
278 establish, i.e. tree rooting strategies are uniformly distributed. During the spin-up simulation local environmental conditions
279 lead to environmental filtering supported by competition and PFT-dominance dependent establishment rates (Sect. 2.2.4).
280 Therefore, the following transient simulations already start with distinct distributions of tree rooting strategies.

281 2.5 Model validation

282 2.5.1 Validation data

283 *Regional biomass pattern*



284 For evaluation of simulated regional pattern of AGB we compare the results of all LPJmL model versions used in this study
285 to two remote sensing based biomass maps (Avitabile et al., 2016a; Saatchi et al., 2011) regridded to the spatial resolution of
286 the LPJmL models.

287 *Inventory-based biomass*

288 Because of the contradicting spatial pattern of currently available AGB maps, we also perform a direct comparison of our
289 modelled AGB patterns to inventory-based biomass estimates provided by (Brienen et al., 2015). The general problem of
290 such a comparison is that AGB estimates from DGVMs represent large-scale (0.5 x 0.5 degree) averages, while inventory-
291 based AGB estimates are representative for forest plots of a typical size of ~1 ha. Because of the smaller spatial scale, plot
292 estimates are affected by spatial variability and random measurement errors (Chave et al., 2004), which causes plot estimates
293 to differ from large-scale average AGB. Thus, even a simulated AGB pattern that perfectly matches the real large-scale
294 pattern would not yield a correlation coefficient of one when compared to small-scale plot observations. To address this
295 problem, we apply the method from Rammig *et al.* (2018), which was specifically developed to compare spatial patterns of
296 simulated large-scale ecosystem properties (Y) to ground-based observations (X). The method assumes that a small scale
297 “point” measurement consists of two components: the large-scale average and a normally-distributed random component
298 originating from small-scale variability and measurement error. The standard deviation of the random component can be
299 estimated from the data by analyzing differences among neighboring observation point, and then be used to obtain an
300 estimate of the standard deviation of the underlying large-scale AGB pattern $\sigma_{x,LS}$ and to calculate a modified correlation
301 coefficient r_{LS} that accounts for differences in the large-scale patterns by removing the diminishing effect of the random
302 component in point observations. The subscript LS for $\sigma_{x,LS}$ and r_{LS} indicates that they represent estimates of the true large-
303 scale variability and the true correlation coefficient of the large-scale patterns. The uncertainty ranges for these two
304 properties as well as for the pattern average \bar{x} (which does not require a correction and therefore no differentiation of ‘large-
305 scale’) are estimated by bootstrapping. For further details on the underlying methodology see (Rammig et al., 2018).

306 For the evaluation of the modeled large-scale AGB pattern (Y) against inventory-based biomass estimates (X) we employ
307 three metrics to detect deviations in important pattern properties: 1. The ratio of means (\bar{y}/\bar{x}) as a measure for the agreement
308 of pattern average. 2. The ratio of standard deviations of large-scale AGB patterns ($\sigma_y/\sigma_{x,LS}$) as a measure for the agreement
309 of pattern amplitude (the differences between grid cells). 3. The modified ‘large-scale’ Pearson correlation coefficient (r_{LS})
310 as a measure for the agreement of large-scale pattern shape (the location of maxima and minima).

311 *Local scale evapotranspiration and productivity*

312 To evaluate the performance of simulated local ET and net ecosystem exchange (NEE) of the LPJmL versions used in this
313 study, we compare Fluxnet eddy covariance measurements of ET at 7 sites and NEE at 3 sites across the study region (Bonal
314 *et al.*, 2008; Saleska *et al.*, 2013, table 3) to respective simulated rates of local ET and NEE. Fluxnet data was downloaded
315 from <https://fluxnet.fluxdata.org> (under DOI: [10.18140/FLX/1440032](https://doi.org/10.18140/FLX/1440032) and DOI: [10.18140/FLX/1440165](https://doi.org/10.18140/FLX/1440165)) in October 2017
316 and from https://daac.ornl.gov/LBA/guides/CD32_Brazil_Flux_Network.html in November 2019.

317 *Continental scale gridded evapotranspiration products and selection of regions*

318 To evaluate the ET over large regions and during a long period (1981-2010), we use three global gridded datasets: Global
319 Land Data Assimilation System Version 2 (Rodell et al., 2004), ERA-Interim/Land (ERA-Interim, Balsamo *et al.*, 2015) and
320 Global Land Evaporation Amsterdam Model v3.2 (GLEAM, Miralles *et al.*, 2011; Martens *et al.*, 2017).

321 GLDAS and ERA-Interim are land-reanalysis products, meaning that they are land surface models forced with meteorological
322 data that has been corrected with observations to give better estimates of land surface variables. The selection of these two
323 products is based on the study of Sörensson and Ruscica (2018), who found that they have a better performance over South
324 America than other reanalysis and satellite-based ET products. GLDAS uses the land surface model Noah (Ek et al., 2003)
325 forced by Princeton meteorological dataset version 2.2 (Sheffield et al., 2006). The soil depth of Noah is 2 m and the model
326 uses four soil layers and vegetation data from University of Maryland (<http://glcf.umd.edu/data/landcover/>). ERA-Interim uses the



327 land surface model HTESSEL (Hydrology-Tiled ECMWF Scheme for Surface Exchanges over Land, Balsamo *et al.*, 2009)
328 forced by ERA-Interim atmospheric data with a GPCP based correction of monthly precipitation. The soil depth of ERAI-L
329 is 2.89 m, the model uses four soil layers and vegetation data from ECOCLIMAP (Masson *et al.*, 2003).
330 GLEAM uses the Priestley-Taylor equation to estimate the potential ET and a set of algorithms with meteorological and
331 vegetation satellite data as input to calculate the actual ET. The version used here, GLEAMv3.2a (Martens *et al.*, 2017,
332 downloaded from <https://www.gleam.eu/#downloads>) uses precipitation input from MSWEP v1.0 (Beck *et al.*, 2017),
333 vegetation cover from the MODIS product MOD44B, remotely sensed Vegetation Optical Index from CCI-LPRM (Liu *et al.*, 2013) and assimilates soil moisture from both remote sensing (ESA CCI SM v2.3, Liu *et al.*, 2012) and land-reanalysis
334 (GLDAS Noah, Rodell *et al.*, 2004).
335

336 For the temporal analysis of ET we used five climatological regions across the study area called Northern South America
337 (NSA), Equatorial Amazon West (EQ W), Equatorial Amazon East (EQ E), Southern Amazon (SAMz), and South American
338 Monsoon System region (SAMS) (see Figure 11f). These regions result from a K-means clustering analysis of the annual
339 cycles of the main drivers of ET: precipitation and surface net radiation (for details see Sörensson and Ruscica, 2018). For
340 the purpose of this study we divided the large EQ region used by Sörensson and Ruscica (2018) in two smaller (EQ W and
341 EQ E) at 60°W, since this is the approximate division between regimes that have a maximum climatological water deficit
342 (MCWD) of around -200 mm per year (EQ W), and of around -500 mm per year (EQ E). MCWD is an indicator of seasonal
343 water stress (see section 2.5.3).

344 The original spatio-temporal resolution of GLDAS and GLEAM is 0.25° x 0.25° while for ERAI-L it is 0.75° x 0.75°.
345 Monthly time series were calculated from daily values for the three datasets. Hereafter, we use the short names GLDAS,
346 ERAI-L and GLEAM for the described reference datasets.

347 *Spatial distribution of vegetation types*

348 To evaluate the regional distribution of simulated biome types in all LPJmL versions we compare our results to satellite-
349 derived vegetation composition maps from ESA Land cover CCI V2.0.7 (Li *et al.*, 2018) reclassified to the PFTs of LPJmL
350 from Forkel *et al.* (2014). In this dataset PFT dominance is indicated by foliage projected cover (FPC) which is also a
351 standard output variable of all LPJmL models enabling a direct comparison of model results.

352 *Spatial pattern of rooting depth*

353 We compare regional patterns of mean rooting depth simulated with LPJmL4.0-VR to a maximum depth of root water
354 uptake map (Fan *et al.*, 2017) regridded to the 0.5° x 0.5° spatial resolution of LPJmL4.0-VR. This product was inversely
355 modelled by taking the dynamically interacting variables soil water supply and plant water demand into account. Here,
356 supply was based on climate, soil properties and topography and demand on plant transpiration deduced from satellite based
357 reanalysis of atmospheric water fluxes and leaf area index (LAI) data.

358 **2.5.2 Validation metrics**

359 Except for inventory biomass all statistical evaluations of model results were based on 1) Pearson Correlation and 2)
360 normalized mean squared error (NME; Kelley *et al.*, 2013). NME is calculated as:

$$361 \quad NME = \frac{\sum_{i=1}^N |y_i - x_i|}{\sum_{i=1}^N |x_i - \bar{x}|} \quad \text{Eq. (9)}$$

362 where y_i is the simulated and x_i the reference value in the grid cell or time step i . \bar{x} is the mean reference value. NME takes
363 the value 0 at perfect agreement, 1 when the model performs as well as the reference mean and values > 2 indicate complete
364 disagreement.



365 2.5.3 Maximum cumulative water deficit as indicator of seasonal water stress

366 For this study we use the maximum cumulative water deficit (MCWD) as an explanatory variable, since it is a widely used
367 indicator for seasonal water stress for studies in South America (Aragão et al., 2007; Lewis et al., 2011; Malhi et al., 2009).
368 MCWD captures the seasonal difference of ET and precipitation in a cumulative way and therefore reveals dry season
369 strength and duration. Here we calculate MCWD on a monthly basis. Therefore, we first calculate the cumulative water
370 deficit CWD_n of each month n as:

$$371 \quad CWD_n = CWD_{n-1} - PET_n + P_n \quad \text{Eq. (10)}$$

372 where PET is the potential monthly ET and P the monthly sum of precipitation. CWD is constrained to values ≤ 0 and is set
373 to 0 at the end of each hydrological year, here the last day of September, as in Lewis *et al.* (2011). We use P from climate
374 input used for model forcing (Sect. 2.3.1) and PET as it is simulated by LPJmL4.0 (Schaphoff et al., 2018) which is only
375 dependent on net surface radiation and air temperature, therefore remaining an explanatory variable independent of
376 vegetation dynamics. We chose this PET over using the commonly used constant ET of 100 mm/month to calculate CWD
377 (Aragão et al., 2007; Lewis et al., 2011; Malhi et al., 2009), because in this way, the CWD better corresponds to the actual
378 climatological conditions in the different LPJmL model versions used in this study (see Sect. 2.4). MCWD is then calculated
379 as:

$$380 \quad MCWD_y = \min(CWD_{October,y-1}, \dots, CWD_{September,y}) \quad \text{Eq. (11)}$$

381 where y indicates the calendrical year.

382 3 Results

383 3.1 Local and regional pattern of tree rooting strategies

384 The results of LPJmL4.0-VR show a high variation in dominance and compositions of tree rooting strategies across the study
385 region. The contribution of each tree rooting strategy to the overall net primary productivity (NPP) appears highly dependent
386 on local environmental conditions. Comparisons at the local scale show that shallow-rooted (deep-rooted) sub-PFTs
387 contribute more to the overall NPP under generally wetter (drier) and less (more) seasonal climate conditions (Fig. 5). At the
388 Fluxnet site MAN K34, which exhibits a mean annual precipitation (MAP) of 2609 mm and a mean MCWD of -222 mm
389 under CRU climate input (2001-2010), the sub-PFT with a maximum rooting depth (D_{95_max}) of 0.5 m contributes most to
390 overall NPP and the whole distribution of NPP weighted D_{95_max} classes shows a mean of 1.52 m (Fig. 5a). At the Fluxnet
391 site STM K67, which exhibits a lower MAP of 2144 mm and a stronger dry season reflected in a mean MCWD of -465 mm,
392 the NPP weighted distribution of D_{95_max} shows a peak at 10 m and a corresponding mean of 10.26 m (Fig. 5b). Since both
393 sites have a soil thickness of 20 m (according to the soil depth input; Sect. 2.3.2) differences in rooting strategy compositions
394 must emerge from climatic differences. It is important to note that D_{95_max} values in Fig. 5 do not necessarily reflect the true
395 achieved rooting depth of each sub-PFT, but the maximum value. For reasons of visual clarity for this figure we kept the
396 bins of the x-axes as chosen in Tab. 1.

397 Based on this NPP information of each sub-PFT in each grid cell we derived maps of mean rooting depth over the whole
398 study region for the time span 2001-2010 for each climate input used in this study (Fig. 6). In contrast to Fig. 5 we computed
399 the mean of the actually achieved D_{95} of each sub-PFT (evergreen and deciduous combined) weighted by the respective
400 relative NPP contribution of each sub-PFT to total forest NPP (we call $\overline{D_{95}}$). The regional pattern of $\overline{D_{95}}$ is a result of
401 environmental filtering and sub-PFT competition, reflecting the effects of climate and sediment thickness. A general East to
402 West gradient of $\overline{D_{95}}$ over the Amazon region follows climatic gradients of precipitation and MCWD (Fig. S1-2) while soil
403 depth (Fig. 4) constrains $\overline{D_{95}}$ especially in the South-eastern Amazon (compare Fig. 4 & 6). In general, areas with higher



404 mean annual rainfall and weaker dry season show lower $\overline{D_{95}}$ and vice versa. This pattern holds true under all climate inputs,
405 with some minor local differences.

406 Focussing on the climatological clusters (see Sect. 2.5.1 and Fig. 9f) under CRU climate input, the western Amazon (EQ-W),
407 with a MAP of 2708 mm and MCWD of -163 mm, displays an overall mean $\overline{D_{95}}$ of 1.14 m and a maximum of 5.47 m,
408 despite considerably deeper soils present. In the Northern, Western and Southern Amazon clusters (NSA, EQ E, SAMz) with
409 lower MAP of 2299, 2190 and 2035 mm and considerably lower MCWD of -488, -438 and -497 mm (meaning higher
410 seasonality), respectively, mean $\overline{D_{95}}$ increases to 2.32, 3.20 and 2.68 m, respectively. Here maximum $\overline{D_{95}}$ values reach 11.97,
411 11.27 and 9.04 m. In the monsoon dominated region (SAMS) displaying the lowest MAP of 1449 mm and MCWD of -649
412 mm, mean $\overline{D_{95}}$ decreases to 1.37 m. The maximum $\overline{D_{95}}$ of this region reaches 11.17 m located at the border to SAMz.

413 Comparing our results to an inversely modelled global gridded product of maximum depth of root water uptake (MDRU;
414 Fan et al. 2017) we find considerable absolute differences to simulated $\overline{D_{95}}$ while overall patterns coincide (Fig. 7). As $\overline{D_{95}}$
415 (Fig. 6) also the original product by Fan et al. (2017) regridded to LPJmL4.0-VR's spatial resolution (Fig. 7a) shows a
416 northwest to southeast gradient of MDRU across the Amazon region. Lowest mean MDRU is found in cluster EQ W with
417 1.38 m, followed by NSA with 2.98 m, SAMz with 5 m, SAMS with 5.47 m and EQ E with 5.88 m. All cluster have a
418 maximum MDRU > 20 m with the highest value found in SAMS with 64.4 m. Fig. 7c shows a difference map between
419 MDRU and simulated $\overline{D_{95}}$ using CRU climate input. Largest differences are found over a wide area (most pronounced in EQ
420 E, SAMz and SAMS) especially where MDRU exceeds $\overline{D_{95}}$. It appeared that for many grid cells in this area MDRU even
421 exceeds the soil depth input used in this study (2.3.2) substantially. To overcome this technical bias we set MDRU to our soil
422 depth input values in cases where MDRU exceeded them (Fig. 7b) to make MDRU and $\overline{D_{95}}$ more comparable. The
423 differences between this adjusted MDRU and $\overline{D_{95}}$ are more likely caused by model architecture than prescribed abiotic
424 limits, enabling for a more meaningful comparison. After this adjustment mean and maximum values of MDRU in the
425 clusters converge to results of LPJmL4.0-VR by decreasing to 1.85 and 14.28 m for NSA, 1.26 and 17.95 m for EQ W, 2.84
426 and 13.47 m for EQ E, 3.28 and 16.57 m for SAMz, and 2.61 and 49.37 m for SAMS. Consequently, the geographical
427 pattern of $\overline{D_{95}}$ and adjusted MDRU shows a better agreement (Fig. 7d). Largest differences remain in north-western NSA,
428 eastern EQ W, along the Amazon River in EQ E and in eastern SAMz where $\overline{D_{95}}$ exceeds MDRU. On the other hand MDRU
429 substantially exceeds $\overline{D_{95}}$ in south-western SAMz and south-western SAMS. These differences might easily emerge from
430 different model settings and assumptions, e.g. related to differences in spatial model resolution, simulated water percolation
431 and underlying vegetation features.

432 The regional validation of $\overline{D_{95}}$ now allows us to generalize which tree rooting strategies occupy which climate space. Using
433 MCWD and MAP to define a climate space we find a clear separation of $\overline{D_{95}}$ (Fig. 8). A core region with deep-rooted forests
434 (mean $\overline{D_{95}} > 4$ m) is found where MCWD ranges between -1300 and -400 and where MAP is at least 1500 mm (see maps of
435 MCWD and MAP in Fig. S1-2) if soil depth allows for it. This core region is surrounded by a small band of medium rooting
436 depth forests (mean $\overline{D_{95}} \sim 2$ -4 m) forming a crescent shape. Rather shallow-rooted forests (mean $\overline{D_{95}} < 2$ m) are found where
437 MAP is less than 1000 mm and MCWD is below -500 mm, i.e. in increasing seasonally dry climates with MAP at the edge
438 to support closed tropical evergreen forest. Shallow-rooted forests are also simulated in very wet conditions where MCWD is
439 greater than -300 mm and MAP is 1200 mm or higher.

440 3.2 Evapotranspiration rates and productivity

441 3.2.1 Local evapotranspiration

442 Differences of intra-annual ET rates between LPJmL4.0, LPJmL4.0-VR and LPJmL4.0-VR-base are most pronounced at
443 Fluxnet sites showing a high seasonality of rainfall (Fig. 9b, e, g and Fig. 10b, e, g). Here, the results of LPJmL4.0-VR show
444 how variable tree rooting strategies lead to a major improvement of matching measured Fluxnet NEE and ET expressed in



445 reduced NME and increased r^2 -values (Table 4 and 5). This improvement arises from an important new model behaviour:
446 Whereas, LPJmL4.0-VR-base and LPJmL4.0 simulate decreasing ET and increasing NEE during dry seasons at these sites,
447 which is anticorrelated to Fluxnet measurements, LPJmL4.0-VR shows the opposite and follows the Fluxnet signals. This
448 means LPJmL4.0-VR's variable rooting strategies buffer precipitation deficits by usage of deep water. Together with a
449 generally lower mean cloud cover during the dry season, this leads to an increase of productivity and ET as suggested by
450 numerous studies (Nemani et al., 2003; da Rocha et al., 2004). Most pronounced improvements are found at STM K67 and
451 STM K83 where NME of ET and NEE drop below or close to 1 and r^2 -values considerably increase compared to the other 2
452 model versions (Table 4-5). For STM K67 r^2 of NEE is higher under LPJmL4.0 and LPJmL4.0-VR-base, but this refers to a
453 significant anti-correlation. At STM K77 (Fig. 9f) the influence of variable rooting strategies is reversely demonstrated. This
454 former rainforest site was converted to pasture before Eddy covariance measurements began. This local land-use at STM
455 K77 is not representative for the respective 0.5° grid cell, and all 3 LPJmL model versions simulate natural forest. In this
456 case, the shallow rooting systems of LPJmL4.0 and LPJmL4.0-VR-base show a better match to ET measurements.
457 Nevertheless, at STM K83, a selectively logged primary forest site which shares the same model grid cell as STM K77 due
458 to their geographical proximity, LPJmL4.0-VR is the only model reproducing increased ET and decreased NEE during the
459 dry season. At sites with weaker to no dry season (Fig. 9c, d, h) differences between model versions become less
460 pronounced, as water availability is more stable throughout the year leading to less variability in ET. Generally, all models
461 show a better match with ET than with NEE, most likely explainable by the fact that DGVMs a) miss or underestimate
462 important mechanisms driving seasonal productivity and respiration and b) have a coarse spatial resolution and therefore
463 miss site specific environmental factors. The latter might also explain why LPJmL4.0-VR overestimates ET at GF GUY in
464 the dry season. Here the soil depth input for the corresponding grid cell most likely exceeds the soil depth at this site, thus
465 the model overestimates rooting depth and resulting ET.

466 3.2.2 Continental Evapotranspiration

467 Results of regional ET are in line with results of site-specific ET. The climatological clusters within the Amazon region
468 which undergo the strongest dry season (EQ E and SAMz) show the largest differences between LPJmL4.0-VR and the other
469 2 models and also here LPJmL4.0-VR shows a higher agreement with validation data (Fig. 11c, d and Table 6).
470 Improvement is largest for EQ E where NME and r^2 show values of 0.62 and 0.91, respectively, whereas the other 2 models
471 show values of NME ≥ 1.92 and $r^2 \leq 0.21$. As expected in NSA and EQ W model differences become less pronounced as
472 annual precipitation deficits are lower and deep rooting systems play a lesser role, but still there is noticeable improvement
473 e.g. in NSA between January and April, where monthly precipitation is lower than during the rest of the year. In the
474 monsoon dominated cluster outside the Amazon region (SAMS) model differences are least pronounced, since shallow
475 rooting forests in LPJmL4.0-VR dominate this area (Fig. 5) which are similar to the forests with constant rooting systems in
476 the other 2 model versions.

477 3.3 Biome distributions

478 The simulated relative dominance of tropical tree PFTs across the study area differs substantially between model versions
479 (Fig. 12). More than half of the grid cells of LPJmL4.0 show the evergreen and deciduous PFTs equally dominant (Fig. 11g-
480 h). Only in areas outside tropical moist climate regions the model shows a clear dominance of the deciduous PFT, whereas
481 e.g. in the Amazon region evergreen and deciduous PFTs co-exist in almost equal abundance. These patterns strongly differ
482 to satellite-derived vegetation composition maps (Fig. 12a-b) and therefore yield in respective comparisons the highest NME
483 values among all models (Table 7). In contrast LPJmL4.0-VR and LPJmL4.0-VR-base show clear dominance patterns of
484 both tropical tree PFTs across the study area (Fig. 12c-f). This can be attributed to the dominance dependent PFT
485 establishment introduced in this study (Sect. 2.2.5) and applied to LPJmL4.0-VR and LPJmL4.0-VR-base, which makes it



486 possible that one PFT (or sub-PFT) can fully outcompete others. Nevertheless, differences between LPJmL4.0-VR and
487 LPJmL4.0-VR-base are quite substantial. In LPJmL4.0-VR-base the tropical evergreen PFT dominates the North-Western
488 Amazon region only, negligibly extending further than the borders of climatological clusters NSA and EQ W combined.
489 Beyond these borders the tropical deciduous PFT is dominating. In contrast, in LPJmL4.0-VR (Fig. 12e-f) the evergreen tree
490 PFT dominance extends closer to its observed borders including EQ E and SAMz, and the deciduous PFT is pushed towards
491 drier and more seasonal climate (including parts of SAMS). Therefore, LPJmL4.0-VR yields lowest NME values in
492 comparison to satellite-derived vegetation composition maps (Table 7).

493 3.4 Aboveground biomass (AGB)

494 3.4.1 Regional AGB pattern

495 The simulated mean AGB pattern (2001-2010) of LPJmL4.0-VR (Fig. 13c) shows how deep water access produces a
496 contiguous high biomass over the Amazon region. Especially towards the borders of the South-Eastern Amazon region in the
497 climatological clusters EQ E and SAMz AGB values appear rather homogenous in contrast to the other 2 model versions
498 (Fig. 13d-e). In connection with the significantly improved underlying vegetation composition (Fig. 12) it is clear that
499 LPJmL4.0-VR is the only model version capable of simulating high AGB evergreen rainforests across the climatic gradient
500 of the Amazon region (Fig. S1-2). This pattern is suggested by one satellite derived AGB product chosen for evaluation of
501 our model results (Saatchi *et al.*, 2011; Fig 12b) which yields a corresponding NME close to 0 (Table 8), even though this is
502 true for all model versions. Surprisingly, for the other AGB validation product (Avitabile *et al.*, 2016b; Fig. 12a) LPJmL4.0-
503 VR-base yields a smaller NME than LPJmL4.0-VR. Taking into account the significantly less accurate underlying
504 vegetation composition of LPJmL4.0-VR-base (Fig. 12) we regard the comparison as obsolete in this context. The same
505 holds true for LPJmL4.0. A known problem with AGB maps for South America is their poor overall agreement especially in
506 the Amazon region (Mitchard *et al.*, 2014), making it hard to interpret such geographical evaluations. The divergence
507 between the 2 AGB evaluation products chosen for this study clearly displays this problem (Fig. 13a-b). Therefore, we also
508 conducted a site specific AGB comparison with results in the following section (Sect. 3.4.2).

509 3.4.2 AGB at specific sites

510 For site specific comparisons of simulated and observed AGB we calculated 3 indicators, 1) the ratio of means (\bar{y}/\bar{x}) as a
511 measure for the agreement of pattern average, 2) the ratio of standard deviations of large-scale AGB patterns ($\sigma_y/\sigma_{x,LS}$) as a
512 measure for the agreement of pattern amplitude (the differences between grid cells), and 3) the modified ‘large-scale’
513 Pearson correlation coefficient (r_{LS}) as a measure for the agreement of large-scale pattern shape (the location of maxima and
514 minima).

515 Fig. 14 shows a site-specific AGB comparison for LPJmL4.0, LPJmL4.0-VR and LPJmL4.0-VR-base for the four climate
516 input data sets used in this study against inventory data from Brienen *et al.* (2015). We find that for all climate datasets,
517 LPJmL4.0 tends to overestimate and LPJmL4.0-VR-base tends to underestimate average AGB across forest plots in the
518 Amazon region. Except for GLDAS, average AGB from LPJmL4.0-VR lies between these two cases, showing the closest
519 match with average AGB derived from forest plots. However, uncertainties in average AGB from forest plots is quite large
520 (as indicated in spread of violine) so that for all but two cases (LPJmL4.0-VR-base with GSWP3 and WATCH+WFDEI)
521 $\bar{y}/\bar{x} = 1$ falls within the 95 % confidence interval of \bar{y}/\bar{x} .

522 With regard to the pattern’s amplitude (σ), we find that for all climate datasets all model versions tend to overestimate AGB
523 differences across the Amazon, but only for LPJmL4.0 with GSWP3 and WATCH+WFDEI unity is outside the 95 %
524 confidence interval of $\sigma_y/\sigma_{x,LS}$. In other words the spatial difference between grid cell biomass is generally larger than
525 observations imply. Nevertheless, pattern amplitude decreases with increasing model complexity (from LPJmL4.0 over



526 LPJmL4.0-VR-base to LPJmL4.0-VR) so that for LPJmL4.0-VR unity falls within the interquartile range of $\sigma_y/\sigma_{x,LS}$ for all
527 climate datasets. Note, however, that for GLDAS median $\sigma_y/\sigma_{x,LS}$ for LPJmL4.0-VR is slightly larger than for LPJmL4.0-
528 VR-base but the 25 % percentile is lower for LPJmL4.0-VR due to the wider uncertainty distribution.
529 Evaluation of the shape of the large-scale average AGB pattern shows that median r_{LS} increases with increasing model
530 complexity. In other words LPJmL4.0-VR matches large scale maxima and minima of biomass across the Amazon forests
531 best. Highest median r_{LS} are found for LPJmL4.0-VR with 0.43 for CRU, GSWP3, and WATCH+WFDEI and 0.51 for
532 GLDAS (upper bounds of the 95 % interval are 0.61 for CRU, 0.68 for GLDAS, and 0.48 for GSWP3 and
533 WATCH+WFDEI).
534 In summary, we conclude that LPJmL4.0-VR reproduces the ‘observed’ large scale AGB pattern in the Amazon in all three
535 relevant aspects (pattern mean, amplitude and shape) better than either of the two other model versions. Still LPJmL4.0-VR
536 cannot completely reproduce all features of the large-scale AGB pattern in the Amazon, which points to bias in model input
537 connected to climate and soil depth as well as insufficient representation of other important processes for modelling carbon
538 dynamics in tropical forests such as tree mortality (Pillet et al., 2018), gap dynamics (Espírito-Santo et al., 2014), and
539 nutrient limitation (Quesada et al., 2012). However, it is important to acknowledge that AGB estimates derived from
540 inventory plots may be subject to large errors and spatial biases themselves (Saatchi et al., 2015).

541 3.5 Belowground biomass

542 Simulations with LPJmL4.0-VR enable an unprecedented analysis of root carbon pools due to the implementation of
543 belowground carbon investment into tree coarse root structures (Sect. 2.2.3). Fig. 15 shows the mean sum (2001-2010) of
544 coarse and fine root carbon pools of tropical evergreen and deciduous tree PFTs under CRU climate over the study region.
545 As expected the pattern follows simulated mean rooting depth (Fig. 6) as coarse root carbon investment increases
546 accordingly. In the Amazon region drier and more seasonal climate selects for sub-PFTs with deeper tree rooting strategies
547 which comes with higher investments into below-ground root structures, implying lower growth rates of these forests
548 compared to wetter and less seasonal regions.

549 4 Discussion

550 This study demonstrates a generalizable approach to improve the representation of tree root system diversity in a DGVM by
551 employing gradual root growth and a trade-off between below- and aboveground carbon investment. A major advance of the
552 new sub-model version LPJmL4.0-VR is that simulations start with a uniform input distribution of tree rooting strategies for
553 each PFT (tropical evergreen and deciduous) in each location, thus ensuring that all tree rooting strategies have the same
554 chance to establish. This uniform distribution then shapes into a local distribution of abundance driven by local
555 environmental conditions and competition (Fig. 5). Therefore, these distributions are not a pre-selected input, but a model
556 output, enabling to investigate patterns like mean rooting depth over the study region (Fig. 6, 7). Since the simulated
557 vegetation can now adjust its root systems to environmental conditions, the quality of simulated biome distributions (Fig. 12)
558 and subsequently the quality of simulated ET and NEE fluxes (Fig. 9-11) and state variables like AGB (Fig. 13-14) is
559 considerably increased.

560 4.1 Climate and soil determine tree rooting strategies

561 Simulated $\overline{D_{95}}$ (Fig. 6) clearly follows climate gradients and soil depth of the study region (Fig. 4, Fig. S1). Our findings are
562 in line with the general ecological expectation and former studies that seasonal water depletion of upper soil layers, as a
563 combination of annual precipitation sums and dry season length and strength, is positively correlated with the rooting depth
564 of tropical evergreen trees (Baker et al., 2009; Ichii et al., 2007; Kleidon and Heimann, 1998, 1999). We also find lower



565 thresholds for MAP and MCWD were \overline{D}_{95} strongly decreases again which can be explained by different mechanisms leading
566 to a regime shift from the evergreen to the deciduous growing strategy as discussed below (see 4.2).
567 In this study, we focus on the NPP weighted mean rooting depth (\overline{D}_{95}) to detect the tree rooting strategies which are most
568 important for water and carbon fluxes (ET, NEE) as well as biomass. The comparisons of mapped mean MDRU of Fan *et al.*
569 (2017) to \overline{D}_{95} (Fig. 9) should be treated with caution as the latter does not necessarily reflect the productivity nor the
570 dominance of certain tree rooting strategies. Fan *et al.* (2017) back-calculate the necessary water uptake depth to meet
571 observed plant productivity derived from satellites while our results are based on DGVM simulations which yield
572 communities of different tree rooting systems. A number of additional general differences of both approaches and underlying
573 assumptions could have easily led to the observed mismatches: 1) Fan *et al.* (2017) use a different soil depth input, i.e.
574 assuming a different physical boundary of maximum rooting depth. Even though we adjusted MDRU of Fan *et al.* (2017) to
575 the soil depth input used in this study (Fig. 8b), this adjustment was only for cases where MDRU exceeds our soil depth
576 input. Therefore, cases where adjusted MDRU exceeds simulated \overline{D}_{95} in Fig. 8d, e.g. in western SAMz, could be caused by a
577 higher soil depth input assumed in Fan *et al.* (2017) for the respective grid cells. 2) LPJmL4.0-VR simulates the growth and
578 competition of (sub-)PFTs on the basis of leaf level photosynthesis and allocation of accumulated carbon. Their traits, such
579 as the rooting strategy, determine performance and subsequently competitiveness. Therefore, competition could lead to a
580 different \overline{D}_{95} as would be expected when considering water supply and demand of each (sub-)PFT alone. 3) Satellite derived
581 productivity of tropical vegetation can be biased, e.g. due to strong cloud cover all year round, potentially leading to biased
582 plant water demand and deduced MDRU. 4) Different water percolation schemes and soil textures in both models lead to
583 different seasonal plant water supply determining MDRU and \overline{D}_{95} . 5) LPJmL4.0-VR does not employ a ground-water model
584 or static ground-water table. By considering ground-water aquifers the simulated dominance of tree rooting strategies and
585 consequently \overline{D}_{95} could locally shift towards lower values, e.g. in the EQ-E and SAMz cluster, if ground-water depth would
586 be lower than the simulated \overline{D}_{95} . Applying a ground-water model in LPJmL4.0-VR is in the focus of future studies. 6) The
587 tropical deciduous PFT of LPJmL4.0-VR avoids water stress during the dry season by shedding its leaves. Therefore the
588 need for deeper roots to withstand a dry season is relatively low. Generally, areas where the deciduous PFT dominates, e.g.
589 the most southwestern part of the study region (Fig. 6), display a low \overline{D}_{95} whereas this area shows amongst the highest
590 values of MDRU in Fan *et al.* (2017). Since deciduous tree types dominate this area also in reality (Fig. 12b), MDRU values
591 might be overestimated. 7) LPJmL4.0-VR does account for tropical tree PFTs only. Bush and shrub PFT types which might
592 be evergreen and gain access to deep water while stem size remains relatively small (Oliveira *et al.*, 2005) are not accounted
593 for. Implementing more general PFTs into LPJmL4.0-VR is in the focus of future studies.
594 For this study we checked the data availability on maximum rooting depth across South America in the TRY database
595 (Kattge *et al.*, 2020; data downloaded September 2019). As it is also shown in Fan *et al.* (2017; Fig. 2) we found the number
596 of sites within the TRY data base where maximum rooting depth has been measured in South America to be very low.
597 Moreover, the number of data entries per site appeared very small, where 33 TRY sites falling within our study area showed
598 a mean of ~9 and a median of 6 data entries, while 15 sites showed ≤ 5 data entries. Therefore, we decided to not include
599 site specific comparisons of rooting depth as it is not clear how representative these measurements are for the local forest
600 communities. Nevertheless, as shown in Fan *et al.* (2017; Fig. 2) measured site-specific maximum rooting depth across the
601 Amazon region seems to follow the expected climatic gradient and gives confidence to our results. More measurements
602 gathered in openly available databases like TRY will help to evaluate future simulation results more sophisticatedly.

603 4.2 Rooting depth influences the distribution of tropical biomes and biomass

604 Seasonal water deficit and annual precipitation are the main determinants of which tree rooting strategies perform best, are
605 able co-exist and outcompete others in LPJmL4.0-VR (Fig. 8). Avoiding seasonal drought stress due to deep roots broadens
606 the geographical extent of simulated tropical evergreen forest. This vegetation type appears to be competitive over a



607 substantially wider climatic range than anticipated when employing the tree rooting strategies of LPJmL4.0. With
608 LPJmL4.0-VR, drier and more seasonal environments now appear suited for the evergreen PFT (Fig. 10). Below certain
609 thresholds of annual precipitation (around 1000 mm) and of MCWD (around -500 mm) mean \overline{D}_{95} decreases again, indicating
610 a transition from the evergreen to the deciduous growing strategy or more open grasslands (Fig. 8). Whether this transition
611 for each of those thresholds is mainly caused by (a) environmental filtering of deep tree rooting strategies, (b) their
612 competitive exclusion by shallow rooted deciduous tree types together with grass PFTs, (c) fire feedbacks or most probably,
613 a combination of all is yet to be determined and in the focus of further studies.

614 The climatic thresholds of vegetation types we find are comparable to thresholds between evergreen forests and savannah
615 found by e.g. Malhi *et al.* (2009) at an annual precipitation of 1500 mm and at an MCWD of -300 mm. The substantially
616 lower MCWD value found in this study can be explained by the differences in calculating CWD. While Malhi *et al.* (2009)
617 assume a constant rate of ET per month of 100 mm, we use the monthly variable PET (Sect. 2.5.3). Since PET often is
618 significantly higher than 100 mm our monthly CWD and therefore MCWD values are respectively lower. Similarly to Malhi
619 *et al.* (2009), Staver, Archibald and Levin (2011) find that evergreen tree cover appears to be bi-modal within a range of
620 MAP of 1000-2500 mm and ascribe this to climate-fire-vegetation feedbacks. Many recent studies investigating potential
621 forest-savanna bi-stability and tipping points of the Amazon region rely solely on such climatic ranges of tropical biomes
622 (Hirota *et al.*, 2011; Wuyts, Champneys and House, 2017; Zemp *et al.*, 2017; Staal *et al.*, 2018; Ciemer *et al.*, 2019). The
623 results of LPJmL4.0-VR show that knowledge on local tree root adaptations is another important explanatory variable of
624 vegetation cover reducing the uncertainty and width of anticipated climatic ranges where evergreen tree cover can be bi-
625 modal. This will help future studies to quantify climate-fire-vegetation feedbacks, forest resilience and potential individual
626 tipping points of forests in the Amazon region in a new way.

627 Especially the current and potential extent of evergreen forests into drier and more seasonal environments can be better
628 explained when considering local adaptations of tree rooting strategies. In these environments an evergreen growing strategy
629 requires deeper root systems to access deep water. Deeper roots require higher BGB investments (Fig. 12) which on the one
630 hand side has a negative effect on productivity, because during growth the allocation of assimilated carbon shifts towards
631 respiring BGB, while investments into productive AGB need to be reduced. On the other hand drier and more seasonal
632 environments show less cloud cover during the dry season (Nemani *et al.*, 2003), enhancing photosynthesis which increases
633 productivity as long as water access is assured (Costa *et al.*, 2010; Wu *et al.*, 2016). The trade-off between AGB and BGB
634 investment most probably leads to a more homogenous AGB pattern across the Amazon region with similar values over a
635 wide climatic range (compare EQ E and SAMz in Fig. 13c-e). This effect is also visible in lower amplitudes and higher
636 correlation in the large scale AGB pattern from different evaluation sites (Fig. 14).

637 In fact comparisons of biomass pattern between all model versions of this study and different biomass products are difficult,
638 since only LPJmL4.0-VR shows a reasonable geographical distribution of underlying biome types across the study area (Fig.
639 12, Table 7). Therefore, differences in biomass are not solely the consequence of different productivities directly related to
640 diversity in tree rooting strategies, but also the consequence of simulated biome type which can be regarded as an indirect
641 effect of diversity in tree rooting strategies. In LPJmL4.0-VR the evergreen growing strategy dominates the entire Amazon
642 region, which is more productive and accumulates more biomass than the deciduous growing strategy. The latter dominates
643 EQ E and SAMz in LPJmL4.0-VR-base and is equally abundant throughout the Amazon region in LPJmL4.0.

644 Concentrating on LPJmL4.0-VR only, the model matches substantially better with the gridded biomass product of Saatchi *et al.*
645 (2011b), since this product shows generally higher biomass values across the Amazon region which are more similar to
646 LPJmL4.0-VR (Table 8). Therefore, the differences in NME are mainly caused by mean biomass values of rainforests across
647 the whole study area rather than pattern divergence. Thus, we argue lowering overall biomass values in LPJmL4.0-VR
648 would improve its match with (Avitabile *et al.*, 2016b) which is a matter of adjusting overall maximum tree mortality rates
649 (see Sect. 2.2.5). Differences to site-specific measurements (Fig. 14) are rather caused by additional factors, such as a) the



650 coarse model resolution leading to a different climate and soil information input than found at specific sites and b)
651 insufficient representation of important processes forcing carbon dynamics in tropical forests such as tree mortality (Pillet et
652 al., 2018), gap dynamics (Espírito-Santo et al., 2014), and nutrient limitation (Quesada et al., 2012).

653 **4.3 Diverse tree rooting strategies improve simulated evapotranspiration and productivity**

654 In LPJmL4.0-VR variable tree rooting strategies decrease the intra-annual variability of ET and maintain high rates of NEE
655 and ET during the dry season in accordance with the intra-annual trends suggested by evaluation data (Fig. 9-11). More than
656 that simulated rates of ET and productivity peak during the dry season in EQ E which is explained by increased solar
657 radiation while trees having access to deep water in the model and in reality (Costa et al., 2010; Wu et al., 2016). While
658 recent parameter optimization against FAPAR data (Forkel et al., 2015) tried to improve the simulated productivity by
659 adjusting phenology pattern in LPJmL4.0, the seasonal offset in simulated ET for Fluxnet sites in the Amazon region
660 remained a challenge (Schaphoff et al., 2018). In this study we can show for the first time on the regional scale how PFTs
661 with variable tree rooting strategies adjust to local environmental conditions and in return improve simulated rates of ET and
662 NEE (Fig. 9-11). Being able to mechanistically reproduce and explain this broad-scale stabilization of water fluxes into the
663 atmosphere has wide implications for DGVM modelling frameworks and simulation of ET as moisture input to the
664 atmosphere in Earth System Models (ESMs). Our approach can help to better quantify the role of forests for local-to-
665 continental scale moisture recycling and to project the fate of forests under future climate and land-use change. The approach
666 presented here is easily applicable for a wide range of DGVMs and ESMs which simulate fine root distribution in a similar
667 way as the LPJmL model family (based on Jackson *et al.*, 1996). A first and easy to implement step for other models could
668 be to prescribe the relative fine root distribution in a spatial explicit way in accordance to the mean rooting depth ($\overline{D_{95}}$)
669 presented in this study.

670 **5 Conclusions**

671 In this study we show for the first time that diverse tree rooting strategies across South-America can indeed explain the
672 spatial distribution of biome types, biomass, as well as the spatial and temporal pattern of the ecosystem fluxes of ET and
673 NEE even when the competition of tree rooting strategies, carbon investment into gradually growing deep roots, and local
674 soil depth are considered. Because LPJmL4.0-VR allows for a whole spectrum of tree rooting strategies, where each strategy
675 has the same theoretical chance to establish in every location, the simulated local distributions of tree rooting strategies are
676 an emergent simulation output which results from local environmental filtering and competition. This enables to estimate
677 mean rooting depth and below-ground biomass on a continental scale as presented here, as well as future estimates of
678 functional diversity of tree rooting strategies. Moreover, we conclude that tree root adaptation is a key explanatory variable
679 to explain forest cover and to estimate the climatic range of potential forest cover bi-stability in connection with climate-fire-
680 vegetation feedbacks in tropical regions. Generally, we are convinced that our approach is of high importance to all
681 modelling frameworks of DGVMs and Earth System Models (ESMs) aiming at quantifying continental scale moisture
682 recycling, forest tipping points and resilience. So far the continental scale importance of local scale tree root adaptations
683 shows that this potential treasure of below-ground functional diversity must be protected not only in the scope of future
684 global change.

685 **6 Code availability**

686 In case of manuscript acceptance all model code and post-processing scripts will be made available. The first author of this
687 manuscript is also willing to share all information with all reviewers upon request.



688 **7 Data availability**

689 In case of manuscript acceptance all simulation data will be made available. The first author of this manuscript is also willing
690 to share all information with all reviewers upon request.

691 **8 Author contribution**

692 All authors helped in conceptualizing the model. BS and WvB developed the model code. BS, WvB, MD, AS, RR, FL, MB,
693 SB, MH, RO, KT conceived the simulation experiments and BS carried them out. BS, MD, AS, RR and JH analysed model
694 output data. BS prepared the manuscript with contributions from all co-authors.

695 **9 Competing interests**

696 The authors declare that they have no conflict of interest.

697 **10 Acknowledgements**

698 BS and KT acknowledge funding from the BMBF- and Belmont Forum-funded project “CLIMAX: Climate services through
699 knowledge co-production: A Euro-South American initiative for strengthening societal adaptation response to extreme
700 events”, FKZ 01LP1610A. MD is funded by the DFG/FAPESP within the IRTG 1740/TRP 2015/50122-0. MH is supported
701 by a grant from Instituto Serrapilheira/Serra 1709-18983. This work used eddy covariance data acquired and shared by the
702 FLUXNET community, including these networks: AmeriFlux, AfriFlux, AsiaFlux, CarboAfrica, CarboEuropeIP,
703 CarboItaly, CarboMont, ChinaFlux, Fluxnet-Canada, GreenGrass, ICOS, KoFlux, LBA, NECC, OzFlux-TERN, TCOS-
704 Siberia, and USCCC. The ERA-Interim reanalysis data are provided by ECMWF and processed by LSCE. The FLUXNET
705 eddy covariance data processing and harmonization was carried out by the European Fluxes Database Cluster, AmeriFlux
706 Management Project, and Fluxdata project of FLUXNET, with the support of CDIAC and ICOS Ecosystem Thematic
707 Center, and the OzFlux, ChinaFlux and AsiaFlux offices.

708 **11 References**

- 709 Allen, C. D., Breshears, D. D. and McDowell, N. G.: On underestimation of global vulnerability to tree mortality and forest
710 die-off from hotter drought in the Anthropocene, *Ecosphere*, 6(8), 1–55, doi:10.1890/ES15-00203.1, 2015.
- 711 Aragão, L. E. O. C., Malhi, Y., Roman-Cuesta, R. M., Saatchi, S., Anderson, L. O. and Shimabukuro, Y. E.: Spatial patterns
712 and fire response of recent Amazonian droughts, *Geophys. Res. Lett.*, 34(7), 1–5, doi:10.1029/2006GL028946, 2007.
- 713 Arora, V. K. and Boer, G. J.: A Representation of Variable Root Distribution in Dynamic Vegetation Models, *Earth Interact.*,
714 7(6), 1–19, doi:10.1175/1087-3562(2003)007<0001:arovrd>2.0.co;2, 2003.
- 715 Avitabile, V., Herold, M., Heuvelink, G. B. M., Lewis, S. L., Phillips, O. L., Asner, G. P., Armston, J., Ashton, P. S., Banin,
716 L., Bayol, N., Berry, N. J., Boeckx, P., de Jong, B. H. J., Devries, B., Girardin, C. A. J., Kearsley, E., Lindsell, J. A., Lopez-
717 Gonzalez, G., Lucas, R., Malhi, Y., Morel, A., Mitchard, E. T. A., Nagy, L., Qie, L., Quinones, M. J., Ryan, C. M., Ferry, S.
718 J. W., Sunderland, T., Laurin, G. V., Gatti, R. C., Valentini, R., Verbeeck, H., Wijaya, A. and Willcock, S.: An integrated
719 pan-tropical biomass map using multiple reference datasets, *Glob. Chang. Biol.*, 22(4), 1406–1420, doi:10.1111/gcb.13139,
720 2016a.
- 721 Avitabile, V., Herold, M., Heuvelink, G. B. M., Lewis, S. L., Phillips, O. L., Asner, G. P., Armston, J., Ashton, P. S., Banin,
722 L., Bayol, N., Berry, N. J., Boeckx, P., de Jong, B. H. J., Devries, B., Girardin, C. A. J., Kearsley, E., Lindsell, J. A., Lopez-
723 Gonzalez, G., Lucas, R., Malhi, Y., Morel, A., Mitchard, E. T. A., Nagy, L., Qie, L., Quinones, M. J., Ryan, C. M., Ferry, S.



- 724 J. W., Sunderland, T., Laurin, G. V., Gatti, R. C., Valentini, R., Verbeeck, H., Wijaya, A. and Willcock, S.: An integrated
725 pan-tropical biomass map using multiple reference datasets, *Glob. Chang. Biol.*, 22(4), 1406–1420, doi:10.1111/gcb.13139,
726 2016b.
- 727 Baker, I. T., Prihodko, L., Denning, A. S., Goulden, M., Miller, S. and Da Rocha, H. R.: Seasonal drought stress in the
728 amazon: Reconciling models and observations, *J. Geophys. Res. Biogeosciences*, 114(1), 1–10, doi:10.1029/2007JG000644,
729 2008.
- 730 Baker, I. T., Prihodko, L., Denning, A. S., Goulden, M., Miller, S. and Da Rocha, H. R.: Seasonal drought stress in the
731 amazon: Reconciling models and observations, *J. Geophys. Res. Biogeosciences*, 114(1), 1–10, doi:10.1029/2007JG000644,
732 2009.
- 733 Balsamo, G., Viterbo, P., Beijaars, A., van den Hurk, B., Hirschi, M., Betts, A. K. and Scipal, K.: A revised hydrology for
734 the ECMWF model: Verification from field site to terrestrial water storage and impact in the integrated forecast system, *J.*
735 *Hydrometeorol.*, 10(3), 623–643, doi:10.1175/2008JHM1068.1, 2009.
- 736 Balsamo, G., Albergel, C., Beljaars, A., Boussetta, S., Brun, E., Cloke, H., Dee, D., Dutra, E., Munõz-Sabater, J.,
737 Pappenberger, F., De Rosnay, P., Stockdale, T. and Vitart, F.: ERA-Interim/Land: A global land surface reanalysis data set,
738 *Hydrol. Earth Syst. Sci.*, 19(1), 389–407, doi:10.5194/hess-19-389-2015, 2015.
- 739 Baudena, M., Dekker, S. C., van Bodegom, P. M., Cuesta, B., Higgins, S. I., Lehsten, V., Reick, C. H., Rietkerk, M.,
740 Scheiter, S., Yin, Z., Zavala, M. A. and Brovkin, V.: Forests, savannas and grasslands: bridging the knowledge gap between
741 ecology and Dynamic Global Vegetation Models, *Biogeosciences Discuss.*, 11(6), 9471–9510, doi:10.5194/bgd-11-9471-
742 2014, 2014.
- 743 Beck, H. E., Van Dijk, A. I. J. M., Levizzani, V., Schellekens, J., Miralles, D. G., Martens, B. and De Roo, A.: MSWEP: 3-
744 hourly 0.25° global gridded precipitation (1979-2015) by merging gauge, satellite, and reanalysis data, *Hydrol. Earth Syst.*
745 *Sci.*, 21(1), 589–615, doi:10.5194/hess-21-589-2017, 2017.
- 746 Becker, A., Finger, P., Meyer-Christoffer, A., Rudolf, B., Schamm, K., Schneider, U. and Ziese, M.: A description of the
747 global land-surface precipitation data products of the Global Precipitation Climatology Centre with sample applications
748 including centennial (trend) analysis from 1901-present, *Earth Syst. Sci. Data*, 5(1), 71–99, doi:10.5194/essd-5-71-2013,
749 2013.
- 750 Best, M. J., Pryor, M., Clark, D. B., Rooney, G. G., Essery, R. L. H., Ménard, C. B., Edwards, J. M., Hendry, M. A.,
751 Porson, A., Gedney, N., Mercado, L. M., Sitch, S., Blyth, E., Boucher, O., Cox, P. M., Grimmond, C. S. B. and Harding, R.
752 J.: The Joint UK Land Environment Simulator (JULES), model description – Part 1: Energy and water fluxes, *Geosci. Model*
753 *Dev.*, 4(3), 677–699, doi:10.5194/gmd-4-677-2011, 2011.
- 754 Bonal, D., Bosc, A., Ponton, S., Goret, J., Burban, B., Gross, P., Bonnefonds, J. M., Elbers, J. A., Longdoz, B., Epron, D.,
755 Guehl, J. and Granier, A.: Impact of severe dry season on net ecosystem exchange in the Neotropical rainforest of French
756 Guiana, , 14(8), 1917–1933 [online] Available from: <https://edepot.wur.nl/1900>, 2008.
- 757 Brien, R. J. W., Phillips, O. L., Feldpausch, T. R., Gloor, E., Baker, T. R., Lloyd, J., Lopez-Gonzalez, G., Monteagudo-
758 Mendoza, A., Malhi, Y., Lewis, S. L., Vásquez Martínez, R., Alexiades, M., Álvarez Dávila, E., Alvarez-Loayza, P.,
759 Andrade, A., Aragaõ, L. E. O. C., Araujo-Murakami, A., Arets, E. J. M. M., Arroyo, L., Aymard C., G. A., Bánki, O. S.,
760 Baraloto, C., Barroso, J., Bonal, D., Boot, R. G. A., Camargo, J. L. C., Castilho, C. V., Chama, V., Chao, K. J., Chave, J.,
761 Comiskey, J. A., Cornejo Valverde, F., Da Costa, L., De Oliveira, E. A., Di Fiore, A., Erwin, T. L., Fauser, S., Forsthofer,
762 M., Galbraith, D. R., Grahame, E. S., Groot, N., Hérault, B., Higuchi, N., Honorio Coronado, E. N., Keeling, H., Killeen, T.
763 J., Laurance, W. F., Laurance, S., Licona, J., Magnussen, W. E., Marimon, B. S., Marimon-Junior, B. H., Mendoza, C.,
764 Neill, D. A., Nogueira, E. M., Núñez, P., Pallqui Camacho, N. C., Parada, A., Pardo-Molina, G., Peacock, J., Penã-Claros,
765 M., Pickavance, G. C., Pitman, N. C. A., Poorter, L., Prieto, A., Quesada, C. A., Ramírez, F., Ramírez-Angulo, H., Restrepo,
766 Z., Roopsind, A., Rudas, A., Salomão, R. P., Schwarz, M., Silva, N., Silva-Espejo, J. E., Silveira, M., Stropp, J., Talbot, J.,



- 767 Ter Steege, H., Teran-Aguilar, J., Terborgh, J., Thomas-Caesar, R., Toledo, M., Torello-Raventos, M., Umetsu, R. K., Van
768 Der Heijden, G. M. F., Van Der Hout, P., Guimarães Vieira, I. C., Vieira, S. A., Vilanova, E., Vos, V. A. and Zagt, R. J.:
769 Long-term decline of the Amazon carbon sink, *Nature*, 519(7543), 344–348, doi:10.1038/nature14283, 2015.
- 770 Brum, M., Vadeboncoeur, M. A., Ivanov, V., Asbjornsen, H., Saleska, S., Alves, L. F., Penha, D., Dias, J. D., Aragão, L. E.
771 O. C., Barros, F., Bittencourt, P., Pereira, L. and Oliveira, R. S.: Hydrological niche segregation defines forest structure and
772 drought tolerance strategies in a seasonal Amazon forest, *J. Ecol.*, 107(1), 318–333, doi:10.1111/1365-2745.13022, 2019.
- 773 Brunner, I., Herzog, C., Dawes, M. A., Arend, M. and Sperisen, C.: How tree roots respond to drought, *Front. Plant Sci.*,
774 6(JULY), 1–16, doi:10.3389/fpls.2015.00547, 2015.
- 775 Canadell, J., Jackson, R. B., Ehleringer, J. R., Mooney, H. A., Sala, O. E. and Schulze, E.-D.: Max rooting depth of
776 vegetation types at the global scale, *Oecologia*, 108, 583–595, doi:10.1007/s10705-016-9812-z, 1996.
- 777 Chave, J., Condit, R., Aguilar, S., Hernandez, A., Lao, S. and Perez, R.: Error propagation and sealing for tropical forest
778 biomass estimates, *Philos. Trans. R. Soc. B Biol. Sci.*, 359(1443), 409–420, doi:10.1098/rstb.2003.1425, 2004.
- 779 Ciemer, C., Boers, N., Hirota, M., Kurths, J., Müller-Hansen, F., Oliveira, R. S. and Winkelmann, R.: Higher resilience to
780 climatic disturbances in tropical vegetation exposed to more variable rainfall, *Nat. Geosci.*, 12(March), doi:10.1038/s41561-
781 019-0312-z, 2019.
- 782 Costa, M. H., Biajoli, M. C., Sanches, L., Malhado, A. C. M., Hutrya, L. R., Da Rocha, H. R., Aguiar, R. G. and De Araújo,
783 A. C.: Atmospheric versus vegetation controls of Amazonian tropical rain forest evapotranspiration: Are the wet and
784 seasonally dry rain forests any different?, *J. Geophys. Res. Biogeosciences*, 115(4), 1–9, doi:10.1029/2009JG001179, 2010.
- 785 Dee, D. P., Uppala, S. M., Simmons, A. J., Berrisford, P., Poli, P., Kobayashi, S., Andrae, U., Balmaseda, M. A., Balsamo,
786 G., Bauer, P., Bechtold, P., Beljaars, A. C. M., van de Berg, L., Bidlot, J., Bormann, N., Delsol, C., Dragani, R., Fuentes, M.,
787 Geer, A. J., Haimberger, L., Healy, S. B., Hersbach, H., Hólm, E. V., Isaksen, I., Kållberg, P., Köhler, M., Matricardi, M.,
788 McNally, A. P., Monge-Sanz, B. M., Morcrette, J. J., Park, B. K., Peubey, C., de Rosnay, P., Tavolato, C., Thépaut, J. N. and
789 Vitart, F.: The ERA-Interim reanalysis: Configuration and performance of the data assimilation system, *Q. J. R. Meteorol.*
790 *Soc.*, 137(656), 553–597, doi:10.1002/qj.828, 2011.
- 791 Ek, M. B., Mitchell, K. E., Lin, Y., Rogers, E., Grunmann, P., Koren, V., Gayno, G. and Tarpley, J. D.: Implementation of
792 Noah land surface model advances in the National Centers for Environmental Prediction operational mesoscale Eta model, *J.*
793 *Geophys. Res. D Atmos.*, 108(22), 1–16, doi:10.1029/2002jd003296, 2003.
- 794 Eshel, A. and Grünzweig, J. M.: Root-shoot allometry of tropical forest trees determined in a large-scale aeroponic system,
795 *Ann. Bot.*, 112(2), 291–296, doi:10.1093/aob/mcs275, 2013.
- 796 Espírito-Santo, F. D. B., Gloor, M., Keller, M., Malhi, Y., Saatchi, S., Nelson, B., Junior, R. C. O., Pereira, C., Lloyd, J.,
797 Frolking, S., Palace, M., Shimabukuro, Y. E., Duarte, V., Mendoza, A. M., López-González, G., Baker, T. R., Feldpausch, T.
798 R., Brienen, R. J. W., Asner, G. P., Boyd, D. S. and Phillips, O. L.: Size and frequency of natural forest disturbances and the
799 Amazon forest carbon balance, *Nat. Commun.*, 5, 1–6, doi:10.1038/ncomms4434, 2014.
- 800 Fan, Y., Miguez-Macho, G., Jobbágy, E. G., Jackson, R. B. and Otero-Casal, C.: Hydrologic regulation of plant rooting
801 depth, *Proc. Natl. Acad. Sci. U. S. A.*, 114(40), 10572–10577, doi:10.1073/pnas.1712381114, 2017.
- 802 Forkel, M., Carvalhais, N., Schaphoff, S., Bloh, W. V., Migliavacca, M., Thurner, M. and Thonicke, K.: Identifying
803 environmental controls on vegetation greenness phenology through model-data integration, *Biogeosciences*, 11(23), 7025–
804 7050, doi:10.5194/bg-11-7025-2014, 2014.
- 805 Forkel, M., Migliavacca, M., Thonicke, K., Reichstein, M., Schaphoff, S., Weber, U. and Carvalhais, N.: Codominant water
806 control on global interannual variability and trends in land surface phenology and greenness, *Glob. Chang. Biol.*, 21(9),
807 3414–3435, doi:10.1111/gcb.12950, 2015.
- 808 Guimberteau, M., Zhu, D., Maignan, F., Huang, Y., Yue, C., Dantec-Nédélec, S., Otlé, C., Jornet-Puig, A., Bastos, A.,
809 Laurent, P., Goll, D., Bowring, S., Chang, J., Guenet, B., Tifafi, M., Peng, S., Krinner, G., Ducharne, A., Wang, F., Wang,



- 810 T., Wang, X., Wang, Y., Yin, Z., Lauerwald, R., Joetzjer, E., Qiu, C., Kim, H. and Ciais, P.: ORCHIDEE-MICT (revision
811 4126), a land surface model for the high-latitudes: model description and validation, *Geosci. Model Dev. Discuss.*, (June), 1–
812 65, doi:10.5194/gmd-2017-122, 2017.
- 813 Harris, I., Jones, P. D., Osborn, T. J. and Lister, D. H.: Updated high-resolution grids of monthly climatic observations - the
814 CRU TS3.10 Dataset, *Int. J. Climatol.*, 34(3), 623–642, doi:10.1002/joc.3711, 2014.
- 815 Hirota, M., Holmgren, M., Van New, E. H. and Scheffer, M.: Global Resilience of Tropical Forest, *Science* (80-),
816 334(October), 232–235, doi:10.1126/science.1210657, 2011.
- 817 Huang, S., Titus, S. J. and Wiens, D. P.: Comparison of nonlinear height–diameter functions for major Alberta tree species,
818 *Can. J. For. Res.*, 22(9), 1297–1304, 1992.
- 819 Huntingford, C., Zelazowski, P., Galbraith, D., Mercado, L. M., Sitch, S., Fisher, R., Lomas, M., Walker, A. P., Jones, C. D.,
820 Booth, B. B. B., Malhi, Y., Hemming, D., Kay, G., Good, P., Lewis, S. L., Phillips, O. L., Atkin, O. K., Lloyd, J., Gloor, E.,
821 Zaragoza-Castells, J., Meir, P., Betts, R., Harris, P. P., Nobre, C., Marengo, J. and Cox, P. M.: Simulated resilience of
822 tropical rainforests to CO₂-induced climate change, *Nat. Geosci.*, 6(4), 268–273, doi:10.1038/ngeo1741, 2013.
- 823 Ichii, K., Hashimoto, H., White, M. A., Potter, C., Hutyrá, L. R., Huete, A. R., Myneni, R. B. and Nemani, R. R.:
824 Constraining rooting depths in tropical rainforests using satellite data and ecosystem modeling for accurate simulation of
825 gross primary production seasonality, *Glob. Chang. Biol.*, 13(1), 67–77, doi:10.1111/j.1365-2486.2006.01277.x, 2007.
- 826 Jackson, R. B., Canadell, J., Ehleringer, J., Mooney, H., Sala, O. and Schulze, E.: A global analysis of root distributions for
827 terrestrial biomes, *Oecologia*, 108, 389–411, 1996.
- 828 Jenik, J.: Roots and root systems in tropical trees, *Trop. trees as living Syst.*, 323, 2010.
- 829 Jobbágy, E. G. and Jackson, R. B.: the Vertical Distribution of Soil Organic Carbon and Its Relation To Climate and
830 Vegetation, *Ecol. Appl.*, 10(2), 423–436, doi:10.1890/1051-0761(2000)010[0423:TVDOSO]2.0.CO;2, 2000.
- 831 Johnson, D. M., Domec, J. C., Carter Berry, Z., Schwantes, A. M., McCulloh, K. A., Woodruff, D. R., Wayne Polley, H.,
832 Wortemann, R., Swenson, J. J., Scott Mackay, D., McDowell, N. G. and Jackson, R. B.: Co-occurring woody species have
833 diverse hydraulic strategies and mortality rates during an extreme drought, *Plant Cell Environ.*, 41(3), 576–588,
834 doi:10.1111/pce.13121, 2018.
- 835 Johnson, M. O., Galbraith, D., Gloor, M., De Deurwaerder, H., Guimberteau, M., Rammig, A., Thonicke, K., Verbeeck, H.,
836 von Randow, C., Monteagudo, A., Phillips, O. L., Brienen, R. J. W., Feldpausch, T. R., Lopez Gonzalez, G., Fauset, S.,
837 Quesada, C. A., Christoffersen, B., Ciais, P., Sampaio, G., Kruijt, B., Meir, P., Moorcroft, P., Zhang, K., Alvarez-Davila, E.,
838 Alves de Oliveira, A., Amaral, I., Andrade, A., Aragao, L. E. O. C., Araujo-Murakami, A., Arets, E. J. M. M., Arroyo, L.,
839 Aymard, G. A., Baraloto, C., Barroso, J., Bonal, D., Boot, R., Camargo, J., Chave, J., Cogollo, A., Cornejo Valverde, F.,
840 Lola da Costa, A. C., Di Fiore, A., Ferreira, L., Higuchi, N., Honorio, E. N., Killeen, T. J., Laurance, S. G., Laurance, W. F.,
841 Licona, J., Lovejoy, T., Malhi, Y., Marimon, B., Marimon, B. H., Matos, D. C. L., Mendoza, C., Neill, D. A., Pardo, G.,
842 Peña-Claros, M., Pitman, N. C. A., Poorter, L., Prieto, A., Ramirez-Angulo, H., Roopsind, A., Rudas, A., Salomao, R. P.,
843 Silveira, M., Stropp, J., ter Steege, H., Terborgh, J., Thomas, R., Toledo, M., Torres-Lezama, A., van der Heijden, G. M. F.,
844 Vasquez, R., Guimarães Vieira, I. C., Vilanova, E., Vos, V. A. and Baker, T. R.: Variation in stem mortality rates determines
845 patterns of above-ground biomass in Amazonian forests: implications for dynamic global vegetation models, *Glob. Chang.*
846 *Biol.*, 22(12), 3996–4013, doi:10.1111/gcb.13315, 2016.
- 847 Kattge, J., Bönnisch, G., Díaz, S., Lavorel, S., Prentice, I. C., Leadley, P., Tautenhahn, S., Werner, G. D. A., Aakala, T. and
848 Abedi, M.: TRY plant trait database–enhanced coverage and open access, *Glob. Chang. Biol.*, 2020.
- 849 Kelley, D. I., Prentice, I. C., Harrison, S. P., Wang, H., Simard, M., Fisher, J. B. and Willis, K. O.: A comprehensive
850 benchmarking system for evaluating global vegetation models, *Biogeosciences*, 10(5), 3313–3340, doi:10.5194/bg-10-3313-
851 2013, 2013.
- 852 Kim, H., Watanabe, E.-C., Chang, K., Yoshimura, Y., Hirabayashi, J., Famiglietti, T. and Oki, T.: Century long observation



- 853 constrained global dynamic downscaling and hydrologic implication, n.d.
- 854 Kim, Y., Knox, R. G., Longo, M., Medvigy, D., Hutyrá, L. R., Pyle, E. H., Wofsy, S. C., Bras, R. L. and Moorcroft, P. R.:
855 Seasonal carbon dynamics and water fluxes in an Amazon rainforest, *Glob. Chang. Biol.*, 18(4), 1322–1334,
856 doi:10.1111/j.1365-2486.2011.02629.x, 2012.
- 857 Kleidon, A. and Heimann, M.: A method of determining rooting depth from a terrestrial biosphere model and its impacts on
858 the global water and carbon cycle, *Glob. Chang. Biol.*, 4(3), 275–286, doi:10.1046/j.1365-2486.1998.00152.x, 1998.
- 859 Kleidon, A. and Heimann, M.: Deep-rooted vegetation, Amazonian deforestation, and climate: Results from a modelling
860 study, *Glob. Ecol. Biogeogr.*, 8(5), 397–405, doi:10.1046/j.1365-2699.1999.00150.x, 1999.
- 861 Kleidon, A. and Heimann, M.: Assessing the role of deep rooted vegetation in the climate system with model simulations:
862 Mechanism, comparison to observations and implications for Amazonian deforestation, *Clim. Dyn.*, 16(2–3), 183–199,
863 doi:10.1007/s003820050012, 2000.
- 864 Langan, L., Higgins, S. I. and Scheiter, S.: Climate-biomes, pedo-biomes or pyro-biomes: which world view explains the
865 tropical forest–savanna boundary in South America?, *J. Biogeogr.*, 44(10), 2319–2330, doi:10.1111/jbi.13018, 2017.
- 866 Lawrence, D. M., Oleson, K. W., Flanner, M. G., Thornton, P. E., Swenson, S. C., Lawrence, P. J., Zeng, X., Yang, Z.-L.,
867 Levis, S., Sakaguchi, K., Bonan, G. B. and Slater, A. G.: Parameterization improvements and functional and structural
868 advances in Version 4 of the Community Land Model, *J. Adv. Model. Earth Syst.*, 3(3), 1–27, doi:10.1029/2011ms000045,
869 2011.
- 870 Lee, J. E., Oliveira, R. S., Dawson, T. E. and Fung, I.: Root functioning modifies seasonal climate, *Proc. Natl. Acad. Sci. U.*
871 *S. A.*, 102(49), 17576–17581, doi:10.1073/pnas.0508785102, 2005.
- 872 Leuschner, C., Moser, G., Bertsch, C., Röderstein, M. and Hertel, D.: Large altitudinal increase in tree root/shoot ratio in
873 tropical mountain forests of Ecuador, *Basic Appl. Ecol.*, 8(3), 219–230, 2007.
- 874 Lewis, S. L., Brando, P. M., Phillips, O. L., Van Der Heijden, G. M. F. and Nepstad, D.: The 2010 Amazon drought, *Science*
875 (80-), 331(6017), 554, doi:10.1126/science.1200807, 2011.
- 876 Li, W., Houghton, R. A., Bontemps, S., MacBean, N., Lamarche, C., Ciais, P., Peng, S. and Defourny, P.: Gross and net land
877 cover changes in the main plant functional types derived from the annual ESA CCI land cover maps (1992–2015), *Earth*
878 *Syst. Sci. Data*, 10(1), 219–234, doi:10.5194/essd-10-219-2018, 2018.
- 879 Liu, L., Peng, S., AghaKouchak, A., Huang, Y., Li, Y., Qin, D., Xie, A. and Li, S.: Broad Consistency Between Satellite and
880 Vegetation Model Estimates of Net Primary Productivity Across Global and Regional Scales, *J. Geophys. Res.*
881 *Biogeosciences*, 123(12), 3603–3616, doi:10.1029/2018JG004760, 2018.
- 882 Liu, Y., Piao, S., Lian, X., Ciais, P. and Smith, W. K.: Seasonal responses of terrestrial carbon cycle to climate variations in
883 CMIP5 models: Evaluation and projection, *J. Clim.*, 30(16), 6481–6503, doi:10.1175/JCLI-D-16-0555.1, 2017.
- 884 Liu, Y. Y., Dorigo, W. A., Parinussa, R. M., De Jeu, R. A. M., Wagner, W., McCabe, M. F., Evans, J. P. and Van Dijk, A. I.
885 J. M.: Trend-preserving blending of passive and active microwave soil moisture retrievals, *Remote Sens. Environ.*,
886 123(October 2006), 280–297, doi:10.1016/j.rse.2012.03.014, 2012.
- 887 Liu, Y. Y., van Dijk, A. I. J. M., McCabe, M. F., Evans, J. P. and de Jeu, R. A. M.: Global vegetation biomass change (1988-
888 2008) and attribution to environmental and human drivers, *Glob. Ecol. Biogeogr.*, 22(6), 692–705, doi:10.1111/geb.12024,
889 2013.
- 890 Malhi, Y., Aragao, L. E. O. C., Galbraith, D., Huntingford, C., Fisher, R., Zelazowski, P., Sitch, S., McSweeney, C. and
891 Meir, P.: Exploring the likelihood and mechanism of a climate-change-induced dieback of the Amazon rainforest, *Proc. Natl.*
892 *Acad. Sci.*, 106(49), 20610–20615, doi:10.1073/pnas.0804619106, 2009.
- 893 Markewitz, D., Devine, S., Davidson, E. A., Brando, P. and Nepstad, D. C.: Soil moisture depletion under simulated drought
894 in the Amazon: Impacts on deep root uptake, *New Phytol.*, 187(3), 592–607, doi:10.1111/j.1469-8137.2010.03391.x, 2010.
- 895 Martens, B., Miralles, D. G., Lievens, H., Van Der Schalie, R., De Jeu, R. A. M., Fernández-Prieto, D., Beck, H. E., Dorigo,



- 896 W. A. and Verhoest, N. E. C.: GLEAM v3: Satellite-based land evaporation and root-zone soil moisture, *Geosci. Model*
897 *Dev.*, 10(5), 1903–1925, doi:10.5194/gmd-10-1903-2017, 2017.
- 898 Masson, V., Champeaux, J. L., Chauvin, F., Meriguet, C. and Lacaze, R.: A global database of land surface parameters at 1-
899 km resolution in meteorological and climate models, *J. Clim.*, 16(9), 1261–1282, doi:10.1175/1520-0442-16.9.1261, 2003.
- 900 Miralles, D. G., Holmes, T. R. H., De Jeu, R. A. M., Gash, J. H., Meesters, A. G. C. A. and Dolman, A. J.: Global land-
901 surface evaporation estimated from satellite-based observations, *Hydrol. Earth Syst. Sci.*, 15(2), 453–469, doi:10.5194/hess-
902 15-453-2011, 2011.
- 903 Mitchard, E. T. A., Feldpausch, T. R., Brienen, R. J. W., Lopez-Gonzalez, G., Monteagudo, A., Baker, T. R., Lewis, S. L.,
904 Lloyd, J., Quesada, C. A., Gloor, M., ter Steege, H., Meir, P., Alvarez, E., Araujo-Murakami, A., Aragão, L. E. O. C.,
905 Arroyo, L., Aymard, G., Banki, O., Bonal, D., Brown, S., Brown, F. I., Cerón, C. E., Chama Moscoso, V., Chave, J.,
906 Comiskey, J. A., Cornejo, F., Corrales Medina, M., Da Costa, L., Costa, F. R. C., Di Fiore, A., Domingues, T. F., Erwin, T.
907 L., Frederickson, T., Higuchi, N., Honorio Coronado, E. N., Killeen, T. J., Laurance, W. F., Levis, C., Magnusson, W. E.,
908 Marimon, B. S., Marimon Junior, B. H., Mendoza Polo, I., Mishra, P., Nascimento, M. T., Neill, D., Núñez Vargas, M. P.,
909 Palacios, W. A., Parada, A., Pardo Molina, G., Peña-Claros, M., Pitman, N., Peres, C. A., Poorter, L., Prieto, A., Ramirez-
910 Angulo, H., Restrepo Correa, Z., Roopsind, A., Roucoux, K. H., Rudas, A., Salomão, R. P., Schiatti, J., Silveira, M., de
911 Souza, P. F., Steininger, M. K., Stropp, J., Terborgh, J., Thomas, R., Toledo, M., Torres-Lezama, A., Van Andel, T. R., van
912 der Heijden, G. M. F., Vieira, I. C. G., Vieira, S., Vilanova-Torre, E., Vos, V. A., Wang, O., Zartman, C. E., Malhi, Y. and
913 Phillips, O. L.: Markedly divergent estimates of Amazon forest carbon density from ground plots and satellites, *Glob. Ecol.*
914 *Biogeogr.*, 23(8), 935–946, doi:10.1111/geb.12168, 2014.
- 915 Mokany, K., Raison, R. J. and Prokushkin, A. S.: Critical analysis of root: Shoot ratios in terrestrial biomes, *Glob. Chang.*
916 *Biol.*, 12(1), 84–96, doi:10.1111/j.1365-2486.2005.001043.x, 2006.
- 917 Nemani, R. R., Keeling, C. D., Hashimoto, H., Jolly, W. M., Piper, S. C., Tucker, C. J., Myneni, R. B. and Running, S. W.:
918 Climate-driven increases in global terrestrial net primary production from 1982 to 1999, *Science* (80-.), 300(5625), 1560–
919 1563, doi:10.1126/science.1082750, 2003.
- 920 Nepstad, D. C., de Carvalho, C. R., Davidson, E. A., Jipp, P. H., Lefebvre, P. A., Negreiros, G. H., da Silva, E. D., Stone, T.
921 A., Trumbore, S. E. and Vieira, S.: The role of deep roots in the hydrological and carbon cycles of Amazonian forests and
922 pastures, *Nature*, 372(6507), 666–669, doi:10.1038/372666a0, 1994.
- 923 New, M., Hulme, M. and Jones, P.: Representing twentieth century space-time climate variability. Part II: development of a
924 1901-1996 monthly grids of terrestrial surface climate, *J. Clim.*, 13, 2217–2238, 2000.
- 925 Nikolova, P. S., Zang, C. and Pretzsch, H.: Combining tree-ring analyses on stems and coarse roots to study the growth
926 dynamics of forest trees: A case study on Norway spruce (*Picea abies* [L.] H. Karst), *Trees - Struct. Funct.*, 25(5), 859–872,
927 doi:10.1007/s00468-011-0561-y, 2011.
- 928 Oliveira, R. S., Bezerra, L., Davidson, E. A., Pinto, F., Klink, C. A., Nepstad, D. C. and Moreira, A.: Deep root function in
929 soil water dynamics in cerrado savannas of central Brazil, *Funct. Ecol.*, 19(4), 574–581, doi:10.1111/j.1365-
930 2435.2005.01003.x, 2005.
- 931 Ostle, N. J., Smith, P., Fisher, R., Ian Woodward, F., Fisher, J. B., Smith, J. U., Galbraith, D., Levy, P., Meir, P., McNamara,
932 N. P. and Bardgett, R. D.: Integrating plant-soil interactions into global carbon cycle models, *J. Ecol.*, 97(5), 851–863,
933 doi:10.1111/j.1365-2745.2009.01547.x, 2009.
- 934 Pelletier, J. D., Broxton, P. D., Hazenberg, P., Zeng, X., Troch, P. A., Niu, G.-Y., Williams, Z., Brunke, M. A. and Gochis,
935 D.: A gridded global data set of soil, intact regolith, and sedimentary deposit thicknesses for regional and global land surface
936 modeling, *J. Adv. Model. Earth Syst.*, 8, 41–65, doi:10.1002/2017MS001065, 2016.
- 937 Pillet, M., Joetzier, E., Belmin, C., Chave, J., Ciais, P., Dourdain, A., Evans, M., Hérault, B., Luysaert, S. and Poulter, B.:
938 Disentangling competitive vs. climatic drivers of tropical forest mortality, *J. Ecol.*, 106(3), 1165–1179, doi:10.1111/1365-



- 939 2745.12876, 2018.
- 940 Poorter, H., Niklas, K. J., Reich, P. B., Oleksyn, J., Poot, P. and Mommer, L.: Biomass allocation to leaves, stems and roots:
941 meta-analyses of interspecific variation and environmental control, *New Phytol.*, 193(1), 30–50, 2012.
- 942 Prentice, I. C., Sykes, M. T. and Cramer, W.: A simulation model for the transient effects of climate change on forest
943 landscapes, *Ecol. Modell.*, 65(1–2), 51–70, 1993.
- 944 Quesada, C. A., Phillips, O. L., Schwarz, M., Czimczik, C. I., Baker, T. R., Patiño, S., Fyllas, N. M., Hodnett, M. G.,
945 Herrera, R., Almeida, S., Alvarez Dávila, E., Arneeth, A., Arroyo, L., Chao, K. J., Dezzeo, N., Erwin, T., Di Fiore, A.,
946 Higuchi, N., Honorio Coronado, E., Jimenez, E. M., Killeen, T., Lezama, A. T., Lloyd, G., López-González, G., Luizão, F.
947 J., Malhi, Y., Monteagudo, A., Neill, D. A., Núñez Vargas, P., Paiva, R., Peacock, J., Peñuela, M. C., Peña Cruz, A., Pitman,
948 N., Priante Filho, N., Prieto, A., Ramírez, H., Rudas, A., Salomão, R., Santos, A. J. B., Schmerler, J., Silva, N., Silveira, M.,
949 Vásquez, R., Vieira, I., Terborgh, J. and Lloyd, J.: Basin-wide variations in Amazon forest structure and function are
950 mediated by both soils and climate, *Biogeosciences*, 9(6), 2203–2246, doi:10.5194/bg-9-2203-2012, 2012.
- 951 Rammig, A., Heinke, J., Hofhansl, F., Verbeeck, H., Baker, T. R., Christoffersen, B., Ciais, P., De Deurwaerder, H.,
952 Fleischer, K., Galbraith, D., Guimberteau, M., Huth, A., Johnson, M., Kruijff, B., Langerwisch, F., Meir, P., Papastefanou, P.,
953 Sampaio, G., Thonicke, K., Von Randow, C., Zang, C. and Rödiger, E.: A generic pixel-to-point comparison for simulated
954 large-scale ecosystem properties and ground-based observations: An example from the Amazon region, *Geosci. Model Dev.*,
955 11(12), 5203–5215, doi:10.5194/gmd-11-5203-2018, 2018.
- 956 Restrepo-Coupe, N., Levine, N. M., Christoffersen, B. O., Albert, L. P., Wu, J., Costa, M. H., Galbraith, D., Imbuzeiro, H.,
957 Martins, G., da Araujo, A. C., Malhi, Y. S., Zeng, X., Moorcroft, P. and Saleska, S. R.: Do dynamic global vegetation
958 models capture the seasonality of carbon fluxes in the Amazon basin? A data-model intercomparison, *Glob. Chang. Biol.*,
959 23(1), 191–208, doi:10.1111/gcb.13442, 2017.
- 960 da Rocha, H. R., Goulden, M. L., Miller, S. D., Menton, M., Pinto, L. D. V. O., Freitas, H. C. De and Figueira Silva E M.,
961 A.: Seasonality of water and heat fluxes over a tropical forest in eastern Amazonia, *Ecol. Appl.*, 14(4), 22–32,
962 doi:10.1890/02-6005, 2004.
- 963 Rodell, M., Houser, P. R., Jambor, U., Gottschalck, J., Mitchell, K., Meng, C.-J., Arsenault, K., Cosgrove, B., Radakovich,
964 J., Bosilovich, M., Entin, J. K., Walker, J. P., Lohmann, D. and Toll, D.: The Global Land Data Assimilation System, *Bull.*
965 *Am. Meteorol. Soc.*, 85(March), 381–394, 2004.
- 966 Saatchi, S., Mascaró, J., Xu, L., Keller, M., Yang, Y., Duffy, P., Espírito-Santo, F., Baccini, A., Chambers, J. and Schimel,
967 D.: Seeing the forest beyond the trees, *Glob. Ecol. Biogeogr.*, 24(5), 606–610, doi:10.1111/geb.12256, 2015.
- 968 Saatchi, S. S., Harris, N. L., Brown, S., Lefsky, M., Mitchard, E. T. A., Salas, W., Zutta, B. R., Buermann, W., Lewis, S. L.,
969 Hagen, S., Petrova, S., White, L., Silman, M. and Morel, A.: Benchmark map of forest carbon stocks in tropical regions
970 across three continents, *Proc. Natl. Acad. Sci.*, 108(24), 9899–9904, doi:10.1073/pnas.1019576108, 2011.
- 971 Saleska, S. R., Da Rocha, H. R., Huete, A. R., Nobre, A. D., Artaxo, P. E. and Shimabukuro, Y. E.: LBA-ECO CD-32 Flux
972 Tower Network Data Compilation, Brazilian Amazon: 1999–2006, , doi:10.3334/ORNDAAC/1174, 2013.
- 973 Schaphoff, S., von Bloh, W., Rammig, A., Thonicke, K., Biemans, H., Forkel, M., Gerten, D., Heinke, J., Jägermeyr, J.,
974 Knauer, J., Langerwisch, F., Lucht, W., Müller, C., Rolinski, S. and Waha, K.: LPJmL4 – a dynamic global vegetation
975 model with managed land – Part 1: Model description, *Geosci. Model Dev.*, 11(4), 1343–1375, doi:10.5194/gmd-11-1343-
976 2018, 2018.
- 977 Sheffield, J., Goteti, G. and Wood, E. F.: Development of a 50-year high-resolution global dataset of meteorological forcings
978 for land surface modeling, *J. Clim.*, 19(13), 3088–3111, doi:10.1175/JCLI3790.1, 2006.
- 979 Shinozaki, K., Yoda, K. and Kira, T.: A quantitative analysis of plant form - The pipe model theory, *Japanese J. Ecol.*, 14(3),
980 1964.
- 981 Smith, B., Wärlind, D., Arneeth, A., Hickler, T., Leadley, P., Siltberg, J. and Zaehle, S.: Implications of incorporating N

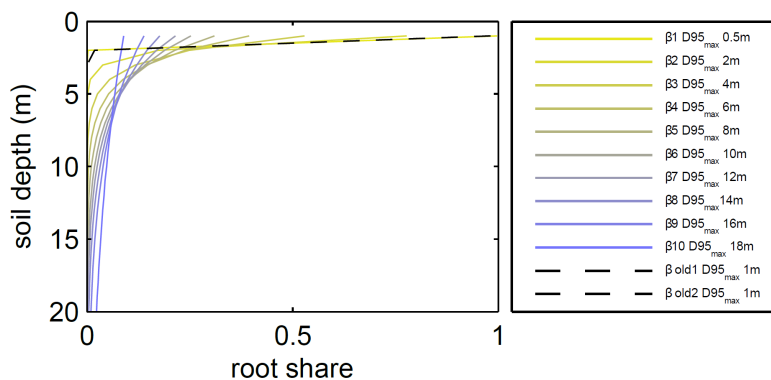


- 982 cycling and N limitations on primary production in an individual-based dynamic vegetation model, *Biogeosciences*, 11(7),
983 2027–2054, doi:10.5194/bg-11-2027-2014, 2014.
- 984 Sörensson, A. A. and Ruscica, R. C.: Intercomparison and Uncertainty Assessment of Nine Evapotranspiration Estimates
985 Over South America, *Water Resour. Res.*, 54(4), 2891–2908, doi:10.1002/2017WR021682, 2018.
- 986 Staal, A., Tuinenburg, O. A., Bosmans, J. H. C., Holmgren, M., Van Nes, E. H., Scheffer, M., Zemp, D. C. and Dekker, S.
987 C.: Forest-rainfall cascades buffer against drought across the Amazon, *Nat. Clim. Chang.*, 8(6), 539–543,
988 doi:10.1038/s41558-018-0177-y, 2018.
- 989 Stahl, C., Hérault, B., Rossi, V., Burban, B., Bréchet, C. and Bonal, D.: Depth of soil water uptake by tropical rainforest
990 trees during dry periods: Does tree dimension matter?, *Oecologia*, 173(4), 1191–1201, doi:10.1007/s00442-013-2724-6,
991 2013.
- 992 Staver, A. C., Archibald, S. and Levin, S. A.: The global extent and determinants of savanna and forest as alternative biome
993 states, *Science* (80-.), 334(6053), 230–232, doi:10.1126/science.1210465, 2011.
- 994 Waring, R. H., Schroeder, P. E. and Oren, R.: Application of the pipe model theory to predict canopy leaf area, *Can. J. For.*
995 *Res.*, 12(3), 556–560, doi:https://doi.org/10.1139/x82-086, 1982.
- 996 Warren, J. M., Hanson, P. J., Iversen, C. M., Kumar, J., Walker, A. P. and Wullschleger, S. D.: Root structural and
997 functional dynamics in terrestrial biosphere models - evaluation and recommendations, *New Phytol.*, 205(1), 59–78,
998 doi:10.1111/nph.13034, 2015a.
- 999 Warren, J. M., Hanson, P. J., Iversen, C. M., Kumar, J., Walker, A. P. and Wullschleger, S. D.: Root structural and
1000 functional dynamics in terrestrial biosphere models - evaluation and recommendations, *New Phytol.*, 205(1), 59–78,
1001 doi:10.1111/nph.13034, 2015b.
- 1002 Weber, U., Jung, M., Reichstein, M., Beer, C., Braakhekke, M. C., Lehsten, V., Ghent, D., Kaduk, J., Viovy, N., Ciais, P.,
1003 Gobron, N. and Rödenbeck, C.: The interannual variability of Africa’s ecosystem productivity: A multi-model analysis,
1004 *Biogeosciences*, 6(2), 285–295, doi:10.5194/bg-6-285-2009, 2009.
- 1005 Weedon, G. P., Gomes, S., Viterbo, P., Shuttleworth, W. J., Blyth, E., Österle, H., Adam, J. C., Bellouin, N., Boucher, O.
1006 and Best, M.: Creation of the WATCH Forcing Data and Its Use to Assess Global and Regional Reference Crop Evaporation
1007 over Land during the Twentieth Century, *J. Hydrometeorol.*, 12(5), 823–848, doi:10.1175/2011jhm1369.1, 2011.
- 1008 Weedon, G. P., Balsamo, G., Bellouin, N., Gomes, S., Best, M. J. and Viterbo, P.: Data methodology applied to ERA-
1009 Interim reanalysis data, *Water Resour. Res.*, 50, 7505–7514, doi:10.1002/2014WR015638, Received, 2014.
- 1010 Wu, J., Albert, L. P., Lopes, A. P., Restrepo-Coupe, N., Hayek, M., Wiedemann, K. T., Guan, K., Stark, S. C.,
1011 Christoffersen, B., Prohaska, N., Tavares, J. V., Marostica, S., Kobayashi, H., Ferreira, M. L., Campos, K. S., Dda Silva, R.,
1012 Brando, P. M., Dye, D. G., Huxman, T. E., Huete, A. R., Nelson, B. W. and Saleska, S. R.: Leaf development and
1013 demography explain photosynthetic seasonality in Amazon evergreen forests, *Science* (80-.), 351(6276), 972–976,
1014 doi:10.1126/science.aad5068, 2016.
- 1015 Wuyts, B., Champneys, A. R. and House, J. I.: Amazonian forest-savanna bistability and human impact, *Nat. Commun.*,
1016 8(May), 1–11, doi:10.1038/ncomms15519, 2017.
- 1017 Xiao, C. W., Yuste, J. C., Janssens, I. A., Roskams, P., Nachtergale, L., Carrara, A., Sanchez, B. Y. and Ceulemans, R.:
1018 Above- and belowground biomass and net primary production in a 73-year-old Scots pine forest, *Tree Physiol.*, 23(8), 505–
1019 516, doi:10.1093/treephys/23.8.505, 2003.
- 1020 Xiao, X., Hagen, S., Zhang, Q., Keller, M. and Moore, B.: Detecting leaf phenology of seasonally moist tropical forests in
1021 South America with multi-temporal MODIS images, *Remote Sens. Environ.*, 103(4), 465–473,
1022 doi:10.1016/j.rse.2006.04.013, 2006.
- 1023 Zemp, D. C., Schleussner, C. F., Barbosa, H. M. J., Hirota, M., Montade, V., Sampaio, G., Staal, A., Wang-Erlandsson, L.
1024 and Rammig, A.: Self-amplified Amazon forest loss due to vegetation-atmosphere feedbacks, *Nat. Commun.*, 8, 1–10,



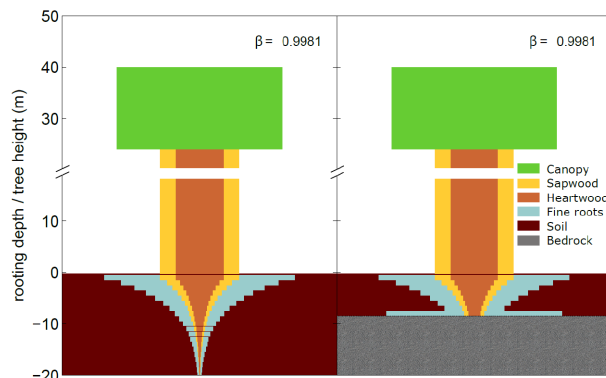
1025 doi:10.1038/ncomms14681, 2017.

1026



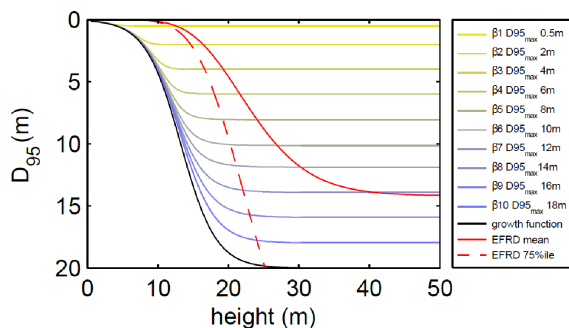
1027

1028 **Figure 1:** Fine root distributions in LPJmL4.0 and fine root distribution at maximum rooting depth in LPJmL4.0-VR as the
 1029 relative amount of fine roots over soil depth. In the legend “ β old1-2” correspond to the β -values of the 2 tropical tree PFTs
 1030 (deciduous and evergreen) employed in LPJmL4.0. The corresponding graphs lie on top of each other due to marginal differences
 1031 in their β -values. “ β 1-10” correspond to the 10 β -values used in LPJmL4.0-VR (table 2) used to create the 10 sub-PFTs of the
 1032 tropical evergreen and deciduous tree PFTs (see 2.2.2). Please note, the first 3 soil layer (as described in 2.2.1) in this visualization
 1033 are treated as 1 layer of 1 m thickness for reasons of visual clarity.



1034

1035 **Figure 2:** Visualization of belowground carbon allocation of a tree PFT in LPJmL4.0-VR with a height of
 1036 40m and a D_{95_max} of 14m (sub-PFT no. 8 in Table 2) growing in a grid cell with a soil depth of 20m (left panel) and a soil depth of
 1037 7m (right panel). As for stem sapwood, also root sapwood needs to satisfy the pipe model. In the first soil layer root sapwood cross-
 1038 sectional area is equal to stem sapwood cross-sectional area, as all water taken up by fine roots needs to pass this layer. In each
 1039 following soil layer the root sapwood cross-sectional area is reduced by the sum of the relative amount of fine roots of all soil layers
 1040 above, thus adjusting the amount of sapwood needed to satisfy the pipe model. Please also see Supplementary Video 1 for a
 1041 visualization of root growth and development of belowground carbon pools over time under [http://www.pik-](http://www.pik-potsdam.de/~borissa/LPJmL4_VR/Supplementary_Video_1.pptx)
 1042 [potsdam.de/~borissa/LPJmL4_VR/Supplementary_Video_1.pptx](http://www.pik-potsdam.de/~borissa/LPJmL4_VR/Supplementary_Video_1.pptx).

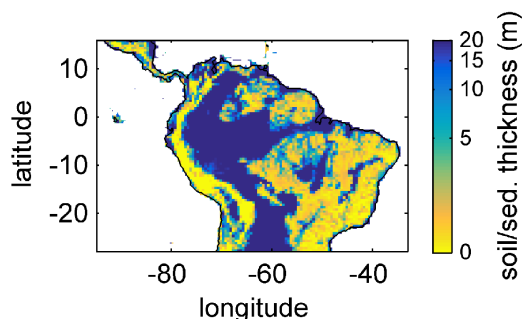


1043

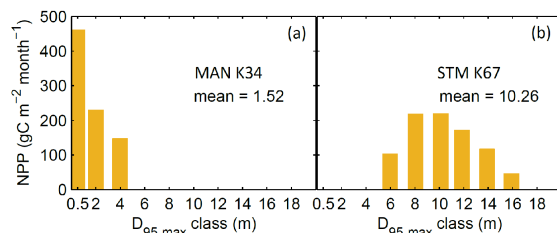
1044 **Figure 3:** Relation between tree height and rooting depth in LPJmL4.0-VR. Black line: Implemented general growth function of
 1045 rooting depth (Eq. 5). Lines with colour scale from yellow to blue: Growth functions of rooting depth for each of the 10 sub-PFTs



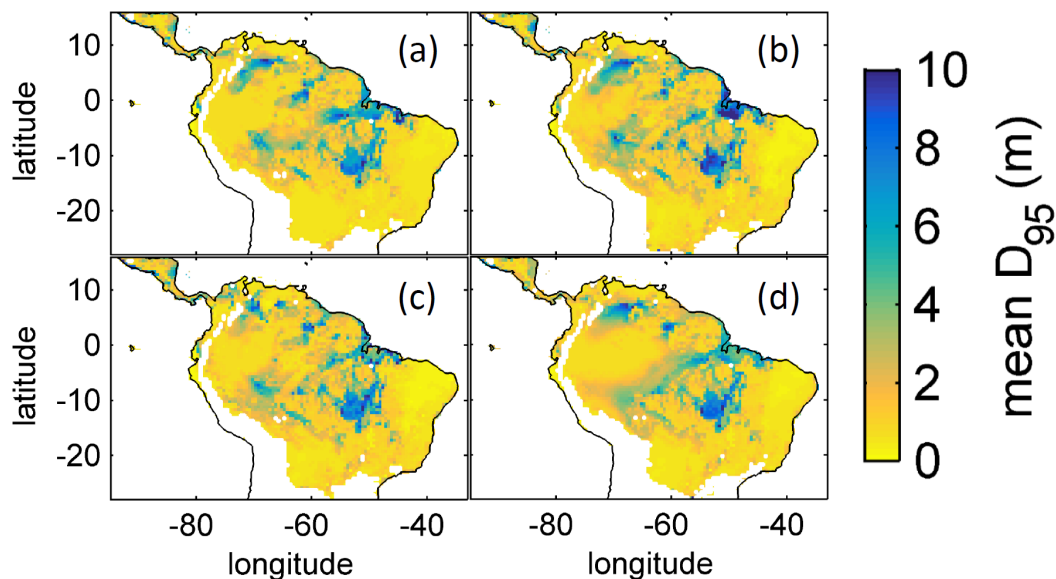
1046 (see 2.2.2). Here temporal rooting depth is expressed as D_{95} and eventually reaches $D_{95,max}$ (Eq. 3). Red solid line: Mean effective
 1047 functional rooting depth over tree height (EFRD) adapted from Brum *et al.* (2019) using Eq. 6. Red dashed line: Respective 75%ile
 1048 EFRD over tree height adapted from Brum *et al.* (2019). Please also see Supplementary Video 1 for a visualization of root growth
 1049 and development of belowground carbon pools over time under [http://www.pik-](http://www.pik-potsdam.de/~borissa/LPJmL4_VR/Supplementary_Video_1.pptx)
 1050 [potsdam.de/~borissa/LPJmL4_VR/Supplementary_Video_1.pptx](http://www.pik-potsdam.de/~borissa/LPJmL4_VR/Supplementary_Video_1.pptx).



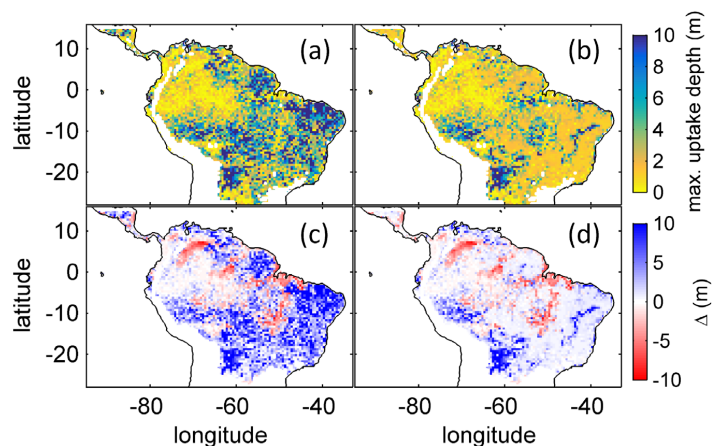
1051
 1052 **Figure 4:** Soil/sediment thickness from (Pelletier *et al.*, 2016) regridded to the $0.5^\circ \times 0.5^\circ$ longitude-latitude grid of LPJmL4.0-VR
 1053 and restricted to a maximum of 20 m. Colorbar in decadic logarithm.



1054
 1055 **Figure 5:** Distributions of simulated mean monthly NPP for each $D_{95,max}$ -class for 2001-2010 under CRU climate input at two
 1056 FluxNet sites. a) Site MAN K34 near the city of Manaus. b) Site STM K67 near the city of Santarem. For more site information see
 1057 table 3 and figure 9a).

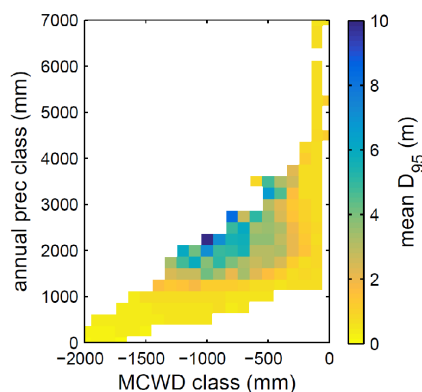


1058
 1059 **Figure 6:** Regional NPP-weighted mean rooting depth ($\overline{D_{95}}$) of all sub-PFTs (evergreen and deciduous combined) for 2001-2010
 1060 and different climate inputs simulated with LPJmL4.0-VR. a) CRU climate input. b) GSWP3 climate input. c) WATCH+WFDEI
 1061 climate input. d) GLDAS climate input. The color scale maximum is set to 10 m.



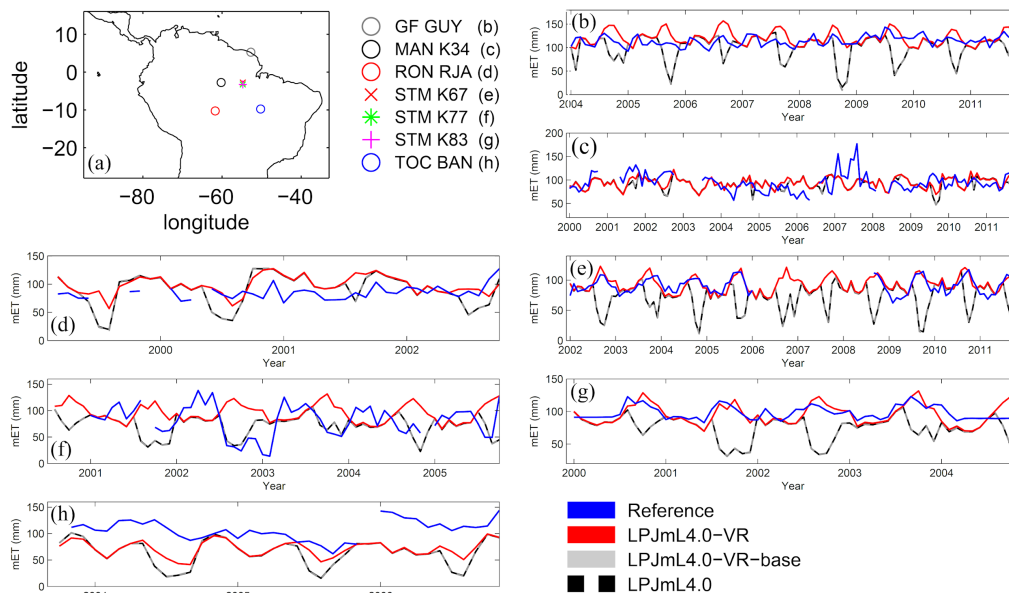
1062

1063 **Figure 7: Comparison of simulated $\overline{D_{95}}$ to product of maximum tree root water uptake depth (MDRU). a) Original (Fan et al.,**
 1064 **2017) MDRU regridded to $0.5^\circ \times 0.5^\circ$ resolution of LPJmL4.0-VR. b) Same as a) but adjusted to soil depth input used in this study**
 1065 **(see 2.3.2), in cases where values of (Fan et al., 2017) exceeded this soil depth. The color scale maximum for a) and b) is set to 10 m.**
 1066 **c) Difference between a) and $\overline{D_{95}}$ simulated with LPJmL4.0-VR under CRU climate forcing (Fig. 6a). d) Difference between b)**
 1067 **and $\overline{D_{95}}$ simulated with LPJmL4.0-VR under CRU climate forcing (Fig. 6a). Red/blue colors denote higher/lower rooting depths**
 1068 **in LPJmL4.0-VR.**



1069

1070 **Figure 8: Mean rooting depth depicted as mean $\overline{D_{95}}$ over classes of MCWD and annual precipitation sums. Class step size for**
 1071 **precipitation was set to 250 mm and class size for MCWD was set to 50 mm. Regions with high amounts of annual rainfall and**
 1072 **lower seasonality exclusively favour shallow rooted forests (low $\overline{D_{95}}$). $\overline{D_{95}}$ increases with decreasing MCWD (increasing seasonal**
 1073 **drought stress) and decreasing sums of annual precipitation. Below 1200 mm of annual rainfall or -1100 mm of MCWD $\overline{D_{95}}$**
 1074 **sharply decreases again. Note this figure does not consider soil depth. The color scale maximum is set to 10 m.**



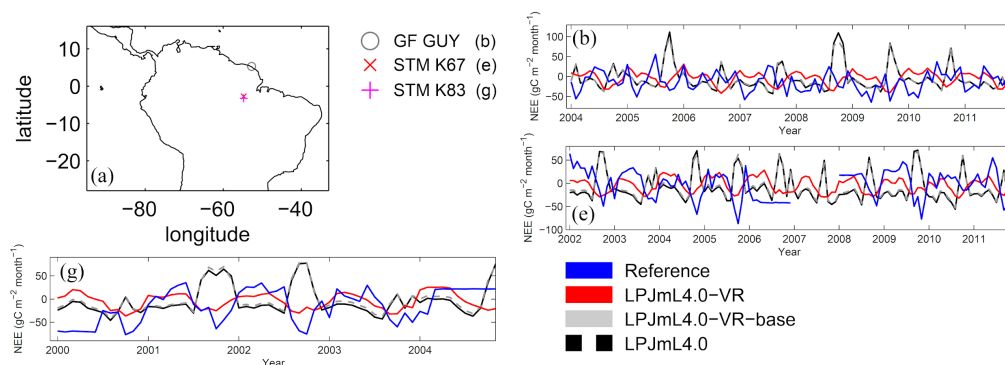
1075

1076

1077

1078

Figure 9: Comparisons of monthly ET between different Fluxnet sites and respective simulation output of the different LPJmL model versions used in this study forced with CRU climate. a) Geographical location of different Fluxnet sites (see also table 3). For statistical measures of the individual comparison see Table 4.



1079

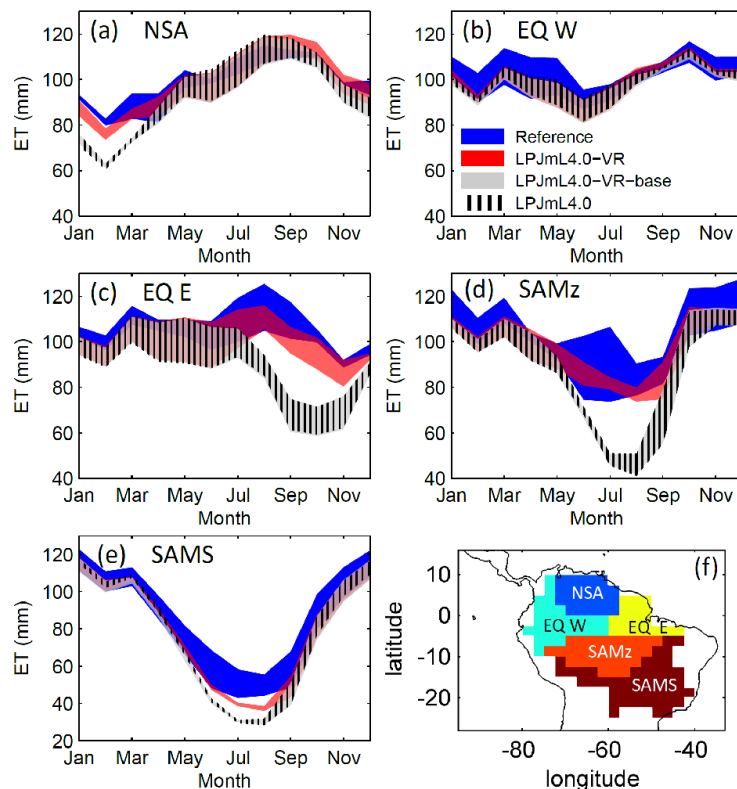
1080

1081

1082

1083

Figure 10: Comparisons of monthly NEE between different Fluxnet sites and respective simulation output of the different LPJmL model versions used in this study forced with CRU climate. a) Geographical location of different Fluxnet sites (see also table 3). For statistical measures of the individual comparison see table 5. Note due to data scarcity only 3 Fluxnet sites are shown. Plots of all sites are shown in Fig. S3. We kept panel labelling as in Fig. 9 to ensure easy comparability.



1084

1085

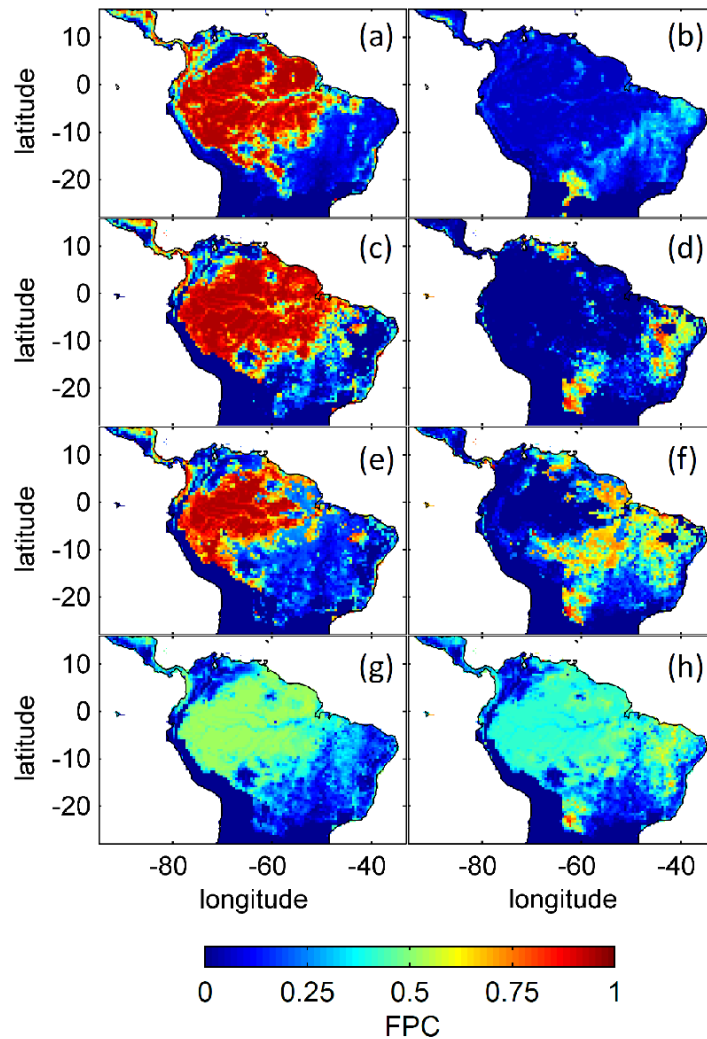
1086

1087

1088

1089

Figure 11: Comparisons of continental scale gridded ET products (2.4.2) against simulated ET within 5 regional climatological clusters (a-e) as defined in 2.4.2). Shown is the mean annual cycle of 1981-2010 and the mean for the whole cluster area. Corridors denote the minimum-maximum range between either the ET products or the model outputs under the different climate forcings used in this study. f) Geographical extent of climatological clusters (adapted from Sörensson and Ruscica, 2018). Statistical measures of the individual comparisons can be found in Table 6 (comparisons of corridor means).



1090

1091

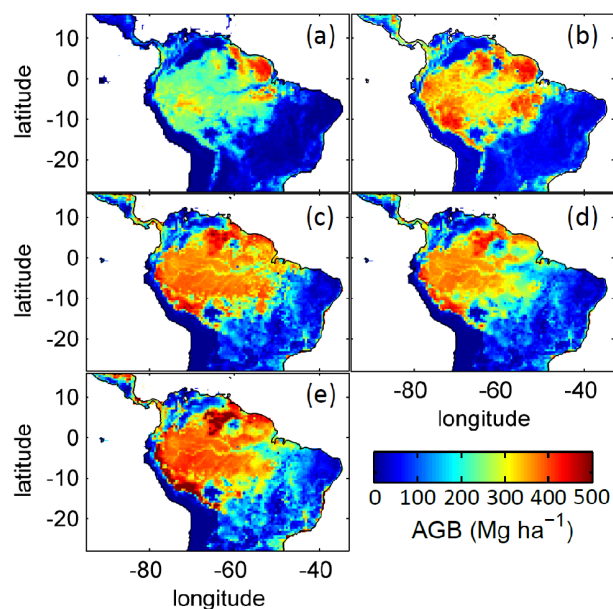
1092

1093

1094

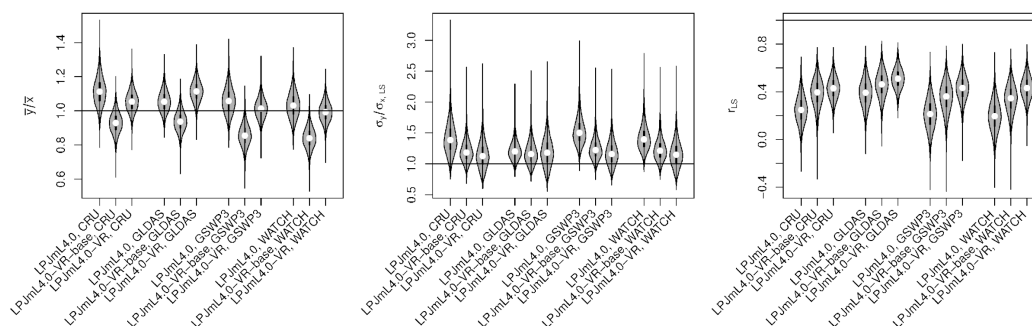
1095

Fig. 12: Foliage projected cover (FPC) of evergreen (a, c, e, g) and deciduous (b, d, f, h) PFTs over the study region. a)-b) Satellite-derived vegetation composition from ESA Land cover CCI V2.0.7 (Li et al., 2018) reclassified to the PFTs of LPJmL as in (Forkel et al., 2014). b)-c) LPJmL4.0-VR. d)-e) LPJmL4.0-VR-base. f)-g) LPJmL4.0. All LPJmL model versions were forced with CRU climate input. The shown FPC for all models refers to 2001-2010. For statistical measures of individual comparisons between model versions (c-h) and satellite derived vegetation composition (a-b) see Table 7.



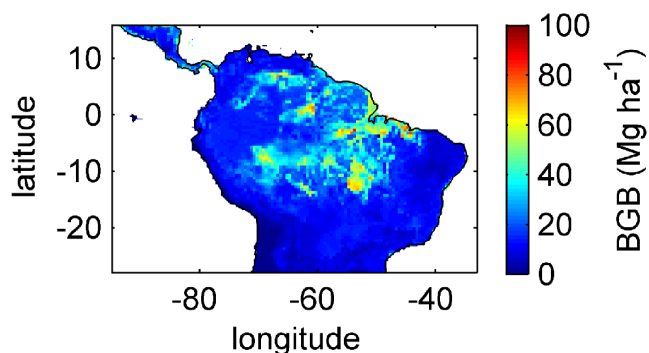
1096
 1097
 1098
 1099
 1100
 1101

Fig. 13: Comparison of simulated AGB and satellite derived AGB validation products regridded to the spatial resolution of LPJmL models. a) Biomass validation product from Avitabile *et al.* (2016b). b) AGB validation product from Saatchi *et al.* (2011). c-e) Mean AGB simulated for the time span 2001-2010 with c) LPJmL4.0-VR. d) LPJmL4.0-VR-base and e) LPJmL4.0. For statistical measures of individual comparisons between model versions (c-e) and satellite derived AGB evaluation products (a-b) see Table 8.



1102
 1103
 1104
 1105
 1106
 1107

Fig. 14: Comparison of simulated large-scale average AGB (Y) from LPJmL4.0, LPJmL4.0-VR-base and LPJmL4.0-VR for different climate datasets to forest inventory data (X) from Brienen *et al.* (2015) using the method from Rammig *et al.* (2019). Three metrics are shown: the ratio of means (\bar{y}/\bar{x}) as a measure for the agreement of pattern average (left), the ratio of standard deviations of large scale AGB patterns ($\sigma_y/\sigma_{x,LS}$) as a measure for the agreement of pattern amplitude (middle), the corrected Pearson correlation coefficient (r_{LS}) as a measure for the agreement of pattern shape (right).



1108

1109 **Fig. 15:** Mean sum (2001-2010) of belowground biomass (BGB; sum of tree coarse and fine roots) of evergreen and deciduous tree
 1110 PFTs simulated with LPJmL4.0-VR under CRU climate forcing.

Soil layer number	Soil layer boundary (m)	Soil layer thickness (m)
1	0.2	0.2
2	0.5	0.3
3	1	0.5
4	2	1
...
23	20	1

1111

1112 **Table 1:** Soil layer partitioning scheme used in LPJmL4.0-VR. The first meter of the soil column is split into 3 soil layers and after
 1113 1m of soil depth each following soil layer is assigned a thickness of 1 m as in LPJmL4.0. Whereas LPJmL4.0's last soil layer
 1114 reaches 3 m, LPJmL4.0-VR's last soil layer reaches 20 m.

sub-PFT number	β -value	D_{95_max} (m)
1	0.9418	0.5
2	0.9851	2
3	0.9925	4
4	0.995	6
5	0.9963	8
6	0.9971	10
7	0.9976	12
8	0.9981	14
9	0.9986	16
10	0.9993	18

1115

1116 **Table 2:** β -values assigned to the 10 sub-PFTs of each tropical PFT (evergreen and deciduous) in LPJmL4.0-VR and the
 1117 corresponding maximum rooting depth reached by 95% of the roots (D_{95_max}).

Site name	Short name	Country	LPJmL coordinate	
			latitude	longitude
Ecotone Bananal Island/BR-Ban	TOC_BAN	Brazil	-9.75	-50.25
Manaus-ZF2 K34/BR-Ma2	MAN_K34	Brazil	-2.75	-60.25
Santarem-Km67-Primary Forest/BR-Sal	STM_K67	Brazil	-2.75	-54.75



Santarem-Km77-Pasture/BR-Sa2	STM_K77	Brazil	-3.25	-54.75
Santarem-Km83-Logged Forest/BR-Sa3	STM_K83	Brazil	-3.25	-54.75
Rond.- Rebio Jaru Ji Parana-Tower B/BR-Ji3	RON_RJA	Brazil	-10.25	-61.75
Guyaflux	GF_GUY	French Guiana	5.25	-52.75

1118

1119 **Table 3: Description of Fluxnet sites used for the evaluation of simulated ET.**

Statistic	Model	TOC BAN	MAN K34	STM K67	STM K77	STM K83	RON RJA	GF GUY
NME	LPJmL4.0-VR	2.41	1.11	0.75	1.38	1.10	2.28	1.57
	LPJmL4.0-VR-base	2.92	1.22	2.29	0.98	2.74	2.73	2.38
	LPJmL4.0	2.93	1.23	2.27	0.98	2.74	2.70	2.36
r ²	LPJmL4.0-VR	0.09	0.03	0.53	0.17	0.43	0.01	0.08
	LPJmL4.0-VR-base	0.10	0.00	0.33	0.14	0.03	0.01	0.01
	LPJmL4.0	0.09	0.00	0.33	0.14	0.03	0.01	0.01
p-value	LPJmL4.0-VR	0.075	0.041	< 0.001	0.002	< 0.001	0.575	0.005
	LPJmL4.0-VR-base	0.067	0.585	< 0.001	0.005	0.221	0.517	0.277
	LPJmL4.0	0.068	0.672	< 0.001	0.005	0.221	0.514	0.274

1120

1121 **Table 4: Normalized mean error (NME), coefficient of determination (r²) and p-value of F-statistic piecewise calculated for simulated ET of the different LPJmL model versions used in this study forced with CRU climate input and Fluxnet data of ET at 7 Fluxnet sites (in accordance with Fig. 8).**

Statistic	Model	STM K67	STM K83	GF GUY
NME	LPJmL4.0-VR	0.90	0.84	1.30
	LPJmL4.0-VR-base	1.62	1.36	1.52
	LPJmL4.0	1.68	1.39	1.52
r ²	LPJmL4.0-VR	0.16	0.14	0.00
	LPJmL4.0-VR-base	0.32	0.06	0.03
	LPJmL4.0	0.33	0.07	0.03
p-value	LPJmL4.0-VR	< 0.001	0.003	0.515
	LPJmL4.0-VR-base	< 0.001	0.055	0.046
	LPJmL4.0	< 0.001	0.047	0.059

1124

1125 **Table 5: Normalized mean error (NME), coefficient of determination (r²) and p-value of F-statistic piecewise calculated for simulated NEE of the different LPJmL model versions used in this study forced with CRU climate input and Fluxnet data of NEE at 3 Fluxnet sites (in accordance with Fig. 10).**

Statistic	Model	NSA	EQ W	EQ E	SAmz	SAMS
NME	LPJmL4.0-VR	0.08	0.26	0.62	0.20	0.06
	LPJmL4.0-VR-base	0.37	0.42	1.95	0.58	0.13
	LPJmL4.0	0.34	0.26	1.92	0.58	0.11
r ²	LPJmL4.0-VR	0.98	0.94	0.91	0.98	1.00
	LPJmL4.0-VR-base	0.94	0.96	0.20	0.91	0.99
	LPJmL4.0	0.93	0.96	0.21	0.90	0.99
p-value	LPJmL4.0-VR	< 0.001	< 0.001	< 0.001	< 0.001	< 0.001
	LPJmL4.0-VR-base	< 0.001	< 0.001	0.143	< 0.001	< 0.001
	LPJmL4.0	< 0.001	< 0.001	0.135	< 0.001	< 0.001

1128

1129 **Table 6: Normalized mean error (NME), coefficient of determination (r²) and p-value of F-statistic piecewise calculated for the simulated ET of the different LPJmL model versions used in this study and continental scale gridded ET products within 5 regional climatological clusters. With respect to Fig. 11 comparisons are based on the monthly mean of corridors shown, i.e. 1) the**

1130

1131



1132 **monthly mean of all outputs produced by one LPJmL model version but forced with different climate inputs and 2) the monthly**
1133 **mean of all continental scale gridded ET data products.**

Statistic	Model	FPC Evergreen	FPC Deciduous
NME	LPJmL4.0-VR	0.31	1.01
	LPJmL4.0-VR-base	0.38	1.5
	LPJmL4.0	0.47	1.76

1134

1135 **Table 7: Normalized mean error (NME) of FPC comparison piecewise calculated between 1) the satellite-derived vegetation**
1136 **composition from ESA Land cover CCI V2.0.7 (Li et al., 2018) reclassified to the PFTs of LPJmL as in Forkel et al. (2014) and 2)**
1137 **all LPJmL model versions used in this study forced with CRU climate data (in accordance with Fig. 10).**

Statistic	Model	Avitabile <i>et al.</i>	Saatchi <i>et al.</i>
NME	LPJmL4.0-VR	0.78	0.12
	LPJmL4.0-VR-base	0.69	0.11
	LPJmL4.0	1.09	0.14

1138

1139 **Table 8: Normalized mean error (NME) of AGB comparison piecewise calculated between 1) the satellite-derived AGB validation**
1140 **products and 2) all LPJmL model versions used in this study forced with CRU climate data (in accordance with Fig. 12).**